Results in Engineering 32 (2026) 111802

Contents lists available at ScienceDirect

Results in Engineering

journal homepage: www.sciencedirect.com/journal/results-in-engineering

Research paper

Comprehensive study of Fe_2MnIn full-heusler alloy: structural, electronic, magnetic, elastic, thermodynamical, and optical properties

Salma Braik [a], Hasan A. Masri [a,*], Nazia Iram [b,*], Mohammed S. Abu-Jafar [a,*], Noorhan F. AlShaikh Mohammad [c], Jihad Asad [c], Mahmoud Farout [a], Mohammed Yasin [d], Aman Kumar [e], Ahmad A. Mousa [f], Saber Saad Essaoud [g]

[a] Department of Physics, An-Najah National University, Nablus, Palestine
[b] Computational Materials Physics Lab, Institute of Physics, Bahauddin Zakariya University, Multan, Pakistan
[c] Department of Physics, Faculty of Applied Sciences, Palestine Technical University, Tulkarm, Palestine
[d] Department of Mathematics, An-Najah National University, Nablus, Palestine
[e] Department of Physics, KVSCOS, Swami Vivekanand Subharti University, Meerut, 250005, India
[f] Middle East University, Amman, 11831, Jordan
[g] Laboratory of Materials and Renewable Energy, Department of Physics, Faculty of Science, University of M'sila, University Pole, Road Bordj Bou-Arreridj, M'sila, 28000, Algeria

ARTICLE INFO

Keywords:
Full Heusler
Ferromagnetic
Elastic
Electronic
Optical

ABSTRACT

This article provides an in-depth study of the Fe_2MnIn full-Heusler alloy, where the FP-LAPW method is used to investigate the interplay between its structural, electronic, magnetic, elastic, and optical properties. To ensure validated results, exchange-correlation effects were treated using the Generalized Gradient Approximation (GGA) and the modified Becke-Johnson (mBJ) potential. The structural analysis indicates that Fe_2MnIn is more stable in the inverse (X_a) phase compared to the normal ($L2_1$) phase. The electronic band structures and density of states have been calculated, that proves material is half-metal in nature. So, it possesses a metallic majority-spin channel and a semiconducting minority-spin channel. Total spin polarization (100%) at the Fermi level is corroborated by the minority band gap widening from 0.1 eV to 0.143 eV through the use of mBJ. Evaluations based on the independent elastic constants C_{11}, C_{12}, and C_{44} indicate that the inverse phase is mechanically stable and ductile, with a Pugh's ratio B/S of 1.873. The optical studies involving spin resolution prove that Fe_2MnIn is also a half-metal and that the material anisotropy is strongly dependent on the orientation of the electron spins. The mBJ functional calculations of the primary absorption of Fe_2MnIn reveal a 0.47 eV blue shifting of primary absorption and a 38% static refractive index increase, which is evidence of spin-polarized anisotropy. Moreover, lattice vibrations were studied by the quasi-harmonic Debye model, and the zero-point energy of this system was 3.74 kJ/mol, and the heat capacity approaches the Dulong-Petit limit at high temperatures.

1. Introduction

An unwavering course of international technical refinement is structurally contingent upon the mass assimilation of high-tier electronics. However, as energy consumption increases due to this evolutionary process, conventional resources and materials increasingly fail to meet global needs [1,2]. Electronic devices that constitute the foundation of the information era function almost exclusively by regulating electron conduction. The charge-centric model was a historical success. Nevertheless, the industry is now witnessing this paradigm reach its ultimate physical limit. The capabilities of standard semiconductor technology are being diminished by core operational constraints. The temperature limit of transistor scaling, the leakage limit of capacitor scaling, and the architectural limit of the von Neumann computing paradigm are identified. Excessive energy consumption and memory instability are detrimental indicators of nanometre scaling that present a significant risk to future technologies [3].

Spintronics has ascended to a position of paramount significance as a transformative paradigm. The major scientific purpose of present technology is to comprehensively eradicate systemic obstacles. The unique

* Corresponding authors.
E-mail addresses: masrihasan223@gmail.com (H.A. Masri), nazia.erum114@gmail.com (N. Iram), mabujafar@najah.edu (M.S. Abu-Jafar).

https://doi.org/10.1016/j.rineng.2026.111802
Received 16 January 2026; Received in revised form 28 April 2026; Accepted 30 June 2026
Available online 30 June 2026

feature of spintronics, compared to traditional electronics, is the utilization of the electron's spin degree of freedom [4]. Non-volatility is no longer a challenge when spin-based architecture is implemented. Furthermore, they enhance the velocity of data processing and significantly decrease the electrical load. The inception of this research area is often traced back to nineteen eighty-eight. This is when Giant Magnetoresistance (GMR) was found in magnetic multilayers by Fert and Gruenberg independently [5]. This discovery showed that electrical resistance is coupled with spin alignment. This led to the development of high-density hard drives and magnetic random-access memory (MRAM) [6]. High-quality performance in spin valves and tunneling magnetoresistance (TMR) junctions is unattainable without a high degree of spin polarization in the constituent materials [7,8]. One of the related alloy and intermetallic systems reports that structural stability and electronic properties are strongly governed by compositional variation and orbital hybridization effects. Arıkan et al. used density functional theory to study the electronic and phonon aspects of full-Heusler alloys X_2YAl. They revealed that variations in composition and orbital hybridization have a big effect on structural stability and electronic behavior [9,10].

Heusler alloys, which have significant potential, were initially identified in 1903 by Dr. Friedrich Heusler. Their distinctive characteristic is the existence of robust ferromagnetism in alloys derived from elements that are non-magnetic in their elemental state [11]. Based on their atomic ratios and lattice symmetry, Heusler alloys are divided into half-Heusler alloys with a $C1^b$ structure and full-Heusler alloys with an $L2_1$ structure [12,13]. Generally, full-Heusler compounds crystallize in the cubic $L2_1$ structure (Fm-3m), with X and Y as transition metals and Z as a p-block element [14]. The flexible nature of the Heusler crystal lattice is responsible for its broad chemical tunability. The engineering of materials with tailored magnetic and electronic properties is achieved by scientists using these techniques.

These compounds are of great interest due to their ability to display superconductivity, topological insulation, and magnetoelasticity [15,16]. Moreover, functionality at room temperature and thermal stability are ensured in full-Heusler alloys by the presence of high Curie temperatures [17]. The thermal properties of Heusler alloys make them indispensable for green energy, going past spintronic needs. Converting waste heat to electricity via the Seebeck effect is the main function of the thermoelectric materials being developed to tackle the modern energy crisis [18]. The thermoelectric figure of merit (ZT) quantifies the performance of these materials. In narrow-gap and semi-metallic Heusler alloys, the ZT values are sufficiently elevated to render them suitable for solid-state cooling and energy generation [19]. Non-centrosymmetric Heusler compounds facilitate the investigation of the spin Hall effect and Bychkov–Rashba effect, enabling the creation of spin currents without external magnetic fields [20].

Despite widespread research into Co-based full-Heusler and Ni-based shape memory alloys, Fe-based alloys are comparatively less understood [21–23]. The particular interest in iron-manganese alloys is specifically on Fe_2MnZ. They are of interest because the complex interaction of Fe and Mn d-electrons can lead to the emergence of diverse magnetic phases and a high level of spin polarization [24–26]. Elastic stability is just as mandatory as electronic functionality for any material used in practical applications. Elastic constants Cij determine how a material distributes and resists external mechanical stress [27–30]. Materials with excellent electronic properties must also be mechanically robust to be used in the aerospace and micro-electro-mechanical systems (MEMS) industries.

Insufficient attention has been compensated to the Fe_2MnIn full-Heusler alloy, placing its physical developments entirely up to speculation. While extensive studies have been conducted on related pnictide systems [31–33], high-precision measurements of the elastic and fundamental physical properties of Fe_2MnIn are completely lacking. Currently, the literature contains no reports on theoretical or experimental work regarding this compound. The lack of experimental and theoretical data keeps Fe_2MnIn virtually untouched. Consequently, the process of experimental synthesis is currently non-predictive in nature, which enshrines a costly trial-and-error methodology as the standard. To fill the literature gap, this study provides the first extensive physical description of Fe_2MnIn using the density functional theory-based linearized augmented plane wave method. The current work provides the first theory of Fe_2MnIn using extensive characterization of the electronic structure, DOS, mechanical moduli, and optical and thermodynamic properties. The results offer a framework for the advancement of iron-based smart materials intended for the creation of next-generation spintronic, optoelectronic, and thermoelectric devices [34].

2. Computational method

An in-depth inquiry into the Fe_2MnIn full Heusler alloy was facilitated by the density functional theory framework [35]. Using a Full Potential Linearized Augmented Plane Wave basis set, the WIEN2k package was applied to calculate a broad range of physical properties for the studied system [36–38]. Structural optimization was first achieved, after which the Generalized Gradient Approximation (GGA) was used to derive the lattice constant along with the bulk modulus. Bandgap values were calculated with improved accuracy by adopting the modified Becke Johnson exchange potential (mBJ) technique [39–41].

To calculate electronic spin in cubic crystals, the spin-polarized SCF method was used. The normal alloys were represented by $L2_1$ (Fm-3m), and the inverse alloys were represented by X_a (F-43m). A muffin-tin radius of 2.13 a.u. was used for Fe, while 2.03 a.u. and 1.93 a.u. were used for Mn and In in the Fe_2MnIn system. For the atoms Fe, Mn, and In in the Fe_2MnIn combination, the muffin-tin radii (R_{MT}) were determined to be 2.13, 2.03, and 1.93 a.u., respectively. The irreducible Brillouin zone for Fe_2MnIn was represented by 24 special k-points. The basis set was characterized by a $K_{MAX}R_{MT}$ value of 8, and a $17 \times 17 \times 17$ full Brillouin zone grid of 5000 k-points was used to extract the data with a 10^{-5} Ry/Bohr convergence. Additionally, l=10 was set for the wavefunction growth inside the muffin-tin spheres. The equilibrium lattice constant and bulk modulus were determined with high accuracy by applying the Murnaghan equation of state [42], to total energy versus volume calculations. providing accurate results through volume relaxation. Total and partial Density of States were calculated to investigate electronic properties, and atomic as well as orbital contributions were identified using x lapw2 -qtl. Brillouin zone integration was carried out using the x tetra program. Subsequently, dosplot was used for the final visualization of the data. Total energy was calculated as a function of small deformations to determine the C_{ij} elastic constants at zero temperature. Seven strain magnitudes, ranging from −3% to +3%, were used for each of the second-rank tensor elastic constants $C_{11}+2C_{12}$, $C_{11}-C_{12}$, and C_{44}. The second derivative of the energy with respect to strain, obtained from a quadratic fit to the energy-strain data, provided the independent elastic constants using cubic-elastic [27,43]. Through the Wien2K optics package, and using the joint density of states, the optical matrix elements were computed [44,45]. Phonon density of states computations within the quasi-harmonic Debye approximation yielded entropy, C_v, U, and F by Quantum Espresso code [46].

3. Results and discussion

3.1. Structural characteristics and thermodynamic stability

The total energy as a function of volume was employed to evaluate the structural stability and ground-state characteristics of the Fe_2MnIn full-Heusler alloy. Crystallisation manifests in two cubic structures. These encompass the Normal $L2_1$ structure (No. 225) and the Inverse X_a structure (No. 216), as illustrated in Fig. 1. The primary distinction between these phases resides in the spatial occupancy of the transition metal atoms, as outlined in Table 1. The $L2_1$ structure has Fe atoms at the 8c Wyckoff sites, whereas Mn and In occupy the 4a and 4b sites, respectively. Structural centro-symmetry of the $L2_1$ phase is absent in

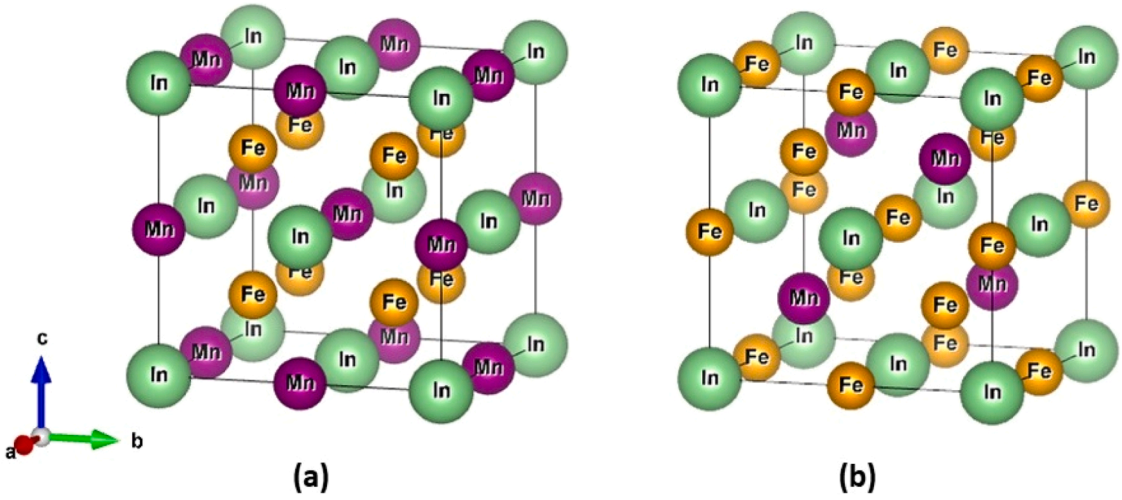

Fig. 1. The crystal structure of (a) normal Fe_2MnIn (b) inverse Fe_2MnIn compounds.

Table 1
Crystallographic, structural, energetic, and elastic parameters of Fe_2MnIn in the normal ($L2_1$) and inverse (X_a) Heusler phases.

Property/Site	Normal Fe_2MnIn ($L2_1$)	Inverse Fe_2MnIn (X_a)
Space group	Fm-3m (No. 225)	F-43m (No. 216)
Fe (site 1)	8c (1/4, 1/4, 1/4)	4a (0, 0, 0)
Fe (site 2)	8c (3/4, 3/4, 3/4)	4c (1/4, 1/4, 1/4)
Mn	4a (0, 0, 0)	4b (1/2, 1/2, 1/2)
In	4b (1/2, 1/2, 1/2)	4d (3/4, 3/4, 3/4)
Equilibrium volume (V_0)	380.40 (a.u.)^3	389.57 (a.u.)^3
Lattice parameter (a)	6.0865 Å	6.1350 Å
Minimum energy (E_0)	−19174.9605 Ry	−19174.9841 Ry
Bulk modulus (B_0)	113.18 GPa	133.64 GPa
Pressure derivative (B′)	2.43	3.59
Formation energy (Ry)	−0.289081	−0.312681

the X_a structure due to Fe occupying 4a and 4c, Mn at 4b, and In at 4d. For the determination of the equilibrium lattice constant (a_0), bulk modulus (B_0), and its first pressure derivative (B′), we fitted the energy-volume (E-V) data to the Murnaghan Equation of State (EOS) [42]:

$$E(V) = E_0(V) + \frac{BV}{B'}\left[\frac{\left(\frac{V_2}{V}\right)^{B'}}{B'-1}+1\right] - \frac{BV_0}{B'-1}, \quad (1)$$

As shown in Fig. 2, the total energy per formula unit is plotted against the volume for both the Normal and Inverse phases of the Fe_2MnIn Heusler alloy. The clear separation between the two parabolas indicates a significant difference in thermodynamic stability. Specifically, the Inverse phase curve reaches a minimum at a much lower energy level than the Normal phase, confirming that the Inverse structure is the ground-state configuration for this material. The curvature of the Inverse phase is also noticeably steeper than that of the Normal phase, which corresponds to its higher resistance to compression.

The total energy change of a physical system during the synthesis of a compound from stable elements defines the formation energy ($E_{form.}$). In computational studies, the $E_{form.}$ is the key descriptor used to predict the chemical and structural stability of a material. The predictive utility of formation energy in the synthesis of Fe_2MnIn is based on the energy of the compound relative to its elements [47].

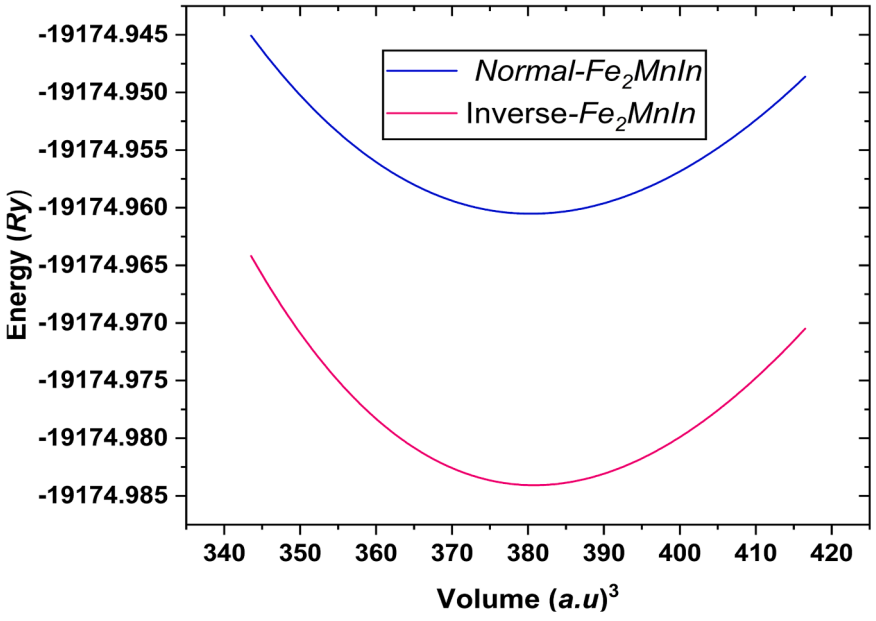

Fig. 2. The variation of total energy with volume for normal Heusler Fe_2MnIn (225) FM and inverse Heusler Fe_2MnIn (216) FM compounds.

$$E_{form.} = E^{Cubic}_{Fe_2MnIn(i)} - \left(2E^{Cubic}_{Fe} + E^{Cubic}_{Mn} + E^{Cubic}_{In}\right) \quad (2)$$

In this study, $E^{Cubic}_{Fe_2MnIn(i)}$ represents the total energy of the Fe_2MnIn compound in its cubic phase, while E^{Cubic}_{Fe}, E^{Cubic}_{Mn},and E^{Cubic}_{In} are the energies associated with the elements Fe, Mn, and In. Two structural configurations are denoted by the specific value of the integer *i*, which is $L2_1$, or X_a. For the Fe_2MnIn Heusler system, the summation of the reference bulk energies for 2Fe, Mn, and In is found to be -19174.671419 Ry. Based on this, the formation energy for the Normal $L2_1$ phase is determined to be -0.289081 Ry, while the formation energy for the Inverse X_a phase is -0.312681 Ry. The negative formation energy for both signifies their stability as compounds; the magnitude implies that the Inverse X_a phase is the more stable component. The table below compares the specific structural and mechanical parameters obtained from the Murnaghan Equation of State (EOS) and the formation energy for both phases.

3.2. Elastic properties

The mechanical resistance of a material against deformation is dictated by its elastic properties, which are indispensable in many applied industries. The mechanical stability of normal Fe_2MnIn was explored by means of density functional theory through the determination of elastic constants C_{ij}. These constants are the vital components needed to build a description of additional mechanical parameters. Using the Reuss approximation framework, the values of bulk modulus B, shear modulus SR, Young's modulus *Y*, Poisson's ratio ν, and anisotropic factor *A* were derived from [48].

$$B = (C_{11} + 2C_{12}) \quad (3)$$

$$S_R = \frac{5C_{44}(C_{11} - C_{12})}{(4C_{44} + 3(C_{11} - C_{12}))} \quad (4)$$

$$Y = \frac{9BS_R}{(S_R + 3B)} \quad (5)$$

$$\nu = \frac{3BS - 2S_R}{2(3B + S_R)} \quad (6)$$

$$A = \frac{2C_{44}}{(C_{11} - C_{12})} \quad (7)$$

The values of the elastic stiffness coefficients C_{ij}, together with the corresponding mechanical moduli for the two structural phases of Fe_2MnIn, are summarized in Table 2. The prerequisite for a cubic crystal to withstand arbitrary infinitesimal strains is the fulfillment of the criteria: $(C_{11} - C_{12}) > 0$, $(C_{11} + 2C_{12}) > 0$, and $C_{44} > 0$ [49]. The inverse Fe_2MnIn phase satisfactorily meets the Born stability criterion; all calculated values from its elastic constants are positive, as seen in the Table 1. The inverse Fe_2MnIn phase shows a positive $C_{11} - C_{12}$ difference of 21.537 GPa, while a negative value of -47.12 GPa is observed for the normal phase. It is confirmed that the inverse (X_a) atomic ordering is preferentially adopted by Fe_2MnIn over the unstable normal Heusler phase.

Table 2
Elastic constants C_{ij} and the associated mechanical features (B, S, Y, v, and A) are analyzed for the Fe_2MnIn Heusler alloy.

Property	Inverse Fe_2MnIn	Normal Fe_2MnIn
C_{11} (*GPa*)	147.516	80.835
C_{12} (GPa)	125.98	127.955
C_{44} (GPa)	111.258	95.752
Bulk Modulus B (GPa)	133.158	—
Shear Modulus S (GPa)	71.062	—
Young's Modulus Y (GPa)	180.99	—
B/S Ratio	1.873	—
Poisson's Ratio ν	0.273	—
Anisotropy Index A	10.332	—

The Pugh's ratio (B/S) is employed here to evaluate the ductile or brittle properties of the stable inverse phase. Based on the empirical Pugh criterion, a material is ductile if its B/S ratio is greater than 1.75 and brittle if it is less than 1.75 [29]. The inverse Fe_2MnIn phase is classified as a ductile material due to its calculated ratio of 1.873 [50]. Poisson's ratio is $\nu = 0.273$, which corroborates the findings by indicating it falls within the metallic regime ($0.25 < \nu < 0.5$) [51].

The characteristics imply that the material is capable of tolerating significant stress during production. The calculated stiffness of 180.990 GPa (Y) demonstrates that the material is suitable for structural applications in microelectronics [29]. However, the directional dependence of the elasticity in Fe_2MnIn is reflected in the high universal anisotropy index (A = 10.332) shown in Table 1 [29,52,53]. Because of the high anisotropy observed, the mechanical response and sound velocities must be accounted for in spintronic heterostructure development.

Fig. 3 provides a thorough assessment of the elastic anisotropy of the Fe_2MnIn inverse Heusler compound, displaying directional representations of Young's modulus, linear compressibility, shear modulus, and Poisson's ratio in both 2D (left column) and 3D (right column) formats.

The two-dimensional projection of Young's modulus in the (xy) plane (Fig. 1a) shows a clear four-lobed (petal-like) deviation from circular symmetry. This means that the stiffness in the plane depends on the direction. The corresponding 3D surface (Fig. 1b), which has a star-like shape with clear protrusions along certain crystallographic directions, confirms this anisotropic behavior even more. These characteristics clearly indicate that stiffness is not consistent across all orientations, exhibiting maximum values in preferred directions and diminished stiffness in others.

In contrast, the linear compressibility profiles (Fig. 1c and d) show almost perfect isotropic properties. The 2D representation makes a circle that is almost perfect, and the 3D surface makes a sphere that is almost perfect. This means that the material's response to hydrostatic pressure is mostly not dependent on direction. This means that the compound can be compressed evenly along all of its crystallographic axes.

The shear modulus behavior (Fig. 1e and f) shows that there is a lot of anisotropy. The 2D plot shows a cross-shaped distribution with sharp peaks in certain directions. The 3D surface, on the other hand, shows pronounced lobes that extend along certain axes. This means that resistance to shear deformation changes a lot depending on the direction. This suggests that some crystallographic orientations are better at withstanding shear stress than others. The strong deviation from spherical symmetry in the shear modulus confirms anisotropic shear behavior.

Ultimately, the distributions of Poisson's ratio (Fig. 1g and h) exhibit intricate multi-lobed designs in both 2D and 3D visuals. The differences in size and form in various directions demonstrate anisotropic transverse strain reactions during uniaxial loading. Significantly, the existence of various lobes with distinct amplitudes indicates that the relationship between axial and lateral deformation is strongly influenced by direction.

In general, although the linear compressibility shows almost perfect isotropy, the Young's modulus, shear modulus, and Poisson's ratio display different levels of anisotropy. The integrated analysis shows that Fe_2MnIn exhibits anisotropic elastic characteristics regarding stiffness, shear resistance, and deformation coupling, while still retaining isotropic volumetric compressibility. These results emphasize the significance of crystallographic orientation in influencing the material's mechanical behavior, which is essential for its possible use in advanced structural and functional systems.

3.3. Magnetic properties

Inconsistencies in the site symmetry of the Fe atoms constitute the most notable difference between the two structural phases. The reported value of 2.38 μB represents the magnetic moment for both equivalent Fe

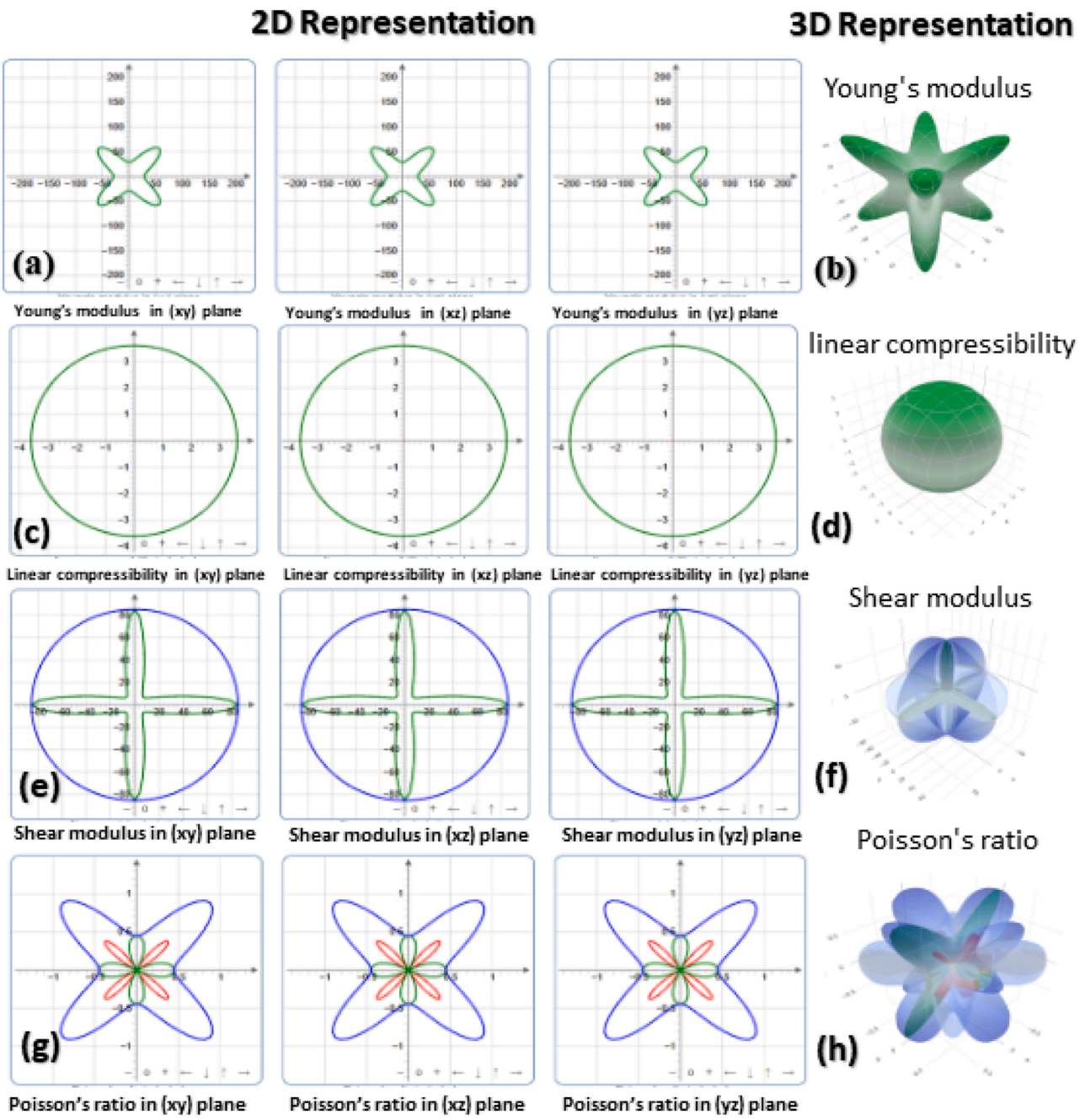

Fig. 3. 2D and 3D anisotropic illustrations of (a-b) Young's Modulus, (c-d) Linear compressibility, (e-f) Shear modulus, and (g-h) Poisson's ratio of Fe_2MnIN-Inverse.

atoms in the normal Fe_2MnIn structure. However, the inverse structure (usually of the X_a type) disturbs this symmetrical condition. While one Fe atom stays at its sublattice, the second atom relocates to Mn. The differentiation into two site types for Fe is the key structural feature responsible for the two different computed moments of 2.49 μB and 2.47 μB. Magnetic exchange is sensitive to geometry, which is suggested by the observed site dependency. The transition from a normal to an inverse structural state is characterized by a drastic expansion of the manganese (Mn) magnetic moment. The magnetic contribution of Mn increases from 2.59 μB in the normal phase to 3.24 μB in the inverse phase. The underlying reason for this enhancement is probably the change in the Mn-Fe interatomic spacing. A decrease in hybridization in the inverse phase likely leads to the Mn d-electron localization being necessary for a larger moment. In the inverse structure, Mtot shows a very evident inclination toward integer values. The total moment of Fe_2MnIn in the inverse phase is 7.99 μB, which is extremely close to 8 μB. The total moment (Mtot) for d-based inverse Heusler alloys is confirmed by the Slater-Pauling rule to follow the Mtot = Nv - 18 mathematical trend [54, 55]. The predicted magnetic moment is 8 μB, with a total count of valence electrons (Nv) = 26, and Fe has 8e- x 2 = 16, Mn 7e-, and In 3e- . At the Fermi level, the material is found to have 100% spin polarization, which is shown by the integer magnetic moment and the consequent insulating properties of one of the spin manifolds. The integer result demonstrates half metallic properties through complete polarization of the electronic structure. A total moment of 7.06 μB is found in the normal phase, indicating that the system is a common metallic ferromagnet without half-metallic properties. In both the normal and inverse structural phases, the indium (In) atoms and the interstitial sites possess negative magnetic moments. These regions are polarized antiparallel to the dominant Fe and Mn moments, which is represented by the negative

sign. The In magnetic moments are small (-0.08 μB to -0.06 μB), characteristic of sp-elements that mainly support the crystal structure. The reduction of the interstitial magnetic moment in the inverse phase (-0.13 μB vs. -0.21 μB) is one factor for the higher total magnetic moment. A high spin polarization level and a stable integer magnetic moment are the foundations for labeling inverse Fe_2MnIn a premier material for STT technology and spin-polarized carrier injection [8].

Although the interatomic magnetic exchange coupling constants were not explicitly calculated, insight into the magnetic exchange interactions can be inferred from the electronic structure and magnetic moment distribution. The well-defined ferromagnetic ground state, together with the near-integer total magnetic moment, indicates strong exchange splitting between majority and minority spin channels, which is a characteristic feature of robust ferromagnetism in Heusler-type systems. The dominant contribution of transition metal ddd-states near the Fermi level suggests that the magnetic interactions are primarily governed by indirect exchange mechanisms, such as double exchange or RKKY-type interactions mediated through conduction electrons. Furthermore, the high spin polarization and absence (or minimal presence) of minority states at the Fermi level support the presence of long-range ferromagnetic coupling. Similar behavior has been reported in related systems, where strong ddd–ddd hybridization stabilizes ferromagnetism even in the absence of explicitly calculated exchange parameters. These observations collectively imply that the magnetic interactions in the present system are sufficiently strong to stabilize the ferromagnetic phase, although a quantitative estimation of exchange constants and Curie temperature would require future investigation using approaches such as the Heisenberg model combined with first-principles calculations (Table 3).

3.4. Electronic properties

A comparative study of GGA and mBJ exchange potentials in DFT was used to investigate the electronic properties of Fe_2MnIn. Fig. 4(a-d) presents the band structures calculated for the spin-polarized full-Heusler alloy. In both models, the spin-up (majority) dispersion shown in Fig. 4(a) and (c) is metallic. Several bands are observed to cross EF, with a high frequency of intersections occurring along the W-L and Γ-X directions. A semiconducting character with a distinct energy gap is exhibited by the spin-down channel in Fig. 4(b) and (d). Under the GGA scheme, the minority channel presents an indirect band gap of 0.1 eV, where the valence band maximum (VBM) is located at the Γ point and the conduction band minimum (CBM) is located at the X point [56].

Fundamental band graph is maintained while the mBJ potential offers a superior description of the electronic states. While the spin-up channel is metallic, the mBJ functional opens the minority-spin gap to 0.143 eV, as shown in Fig. 4(d). In spite of the mBJ bandgap widening, the valence band maximum and conduction band minimum are static near the W point, as per GGA. The direct nature of the gap is confirmed by both approximations. The increase in the gap size with mBJ is typical for Heusler alloys, as standard GGA often underestimates the semiconducting gap in the minority channel because of the lack of proper exchange-correlation treatment for localized d-electrons [41]. The simultaneous occurrence of metallic majority spins and semiconducting minority spins indicates the half-metallicity of Fe_2MnIn.

Table 3
Magnetic moments of Fe_2MnIn phases.

Property/Structure	Normal Phase ($L2_1$)	Inverse Phase (X_a)
Fe Moment (μB)	2.38	2.49
Fe Moment (μB)	2.38	2.47
Mn Moment (μB)	2.59	3.24
In Moment (μB)	−0.08	−0.06
Interstitial Moment (μB)	−0.21	−0.13
Total Moment (μB)	7.06	≈8.00

For spintronic applications, this electronic configuration is of great importance due to its theoretical 100% spin polarization at the Fermi level [57]. Hence, Fe_2MnIn is a material of enormous potential for developing effective spin polarizers, magnetic tunnel junctions, and next-iteration non-volatile spintronic memory. The uniform prediction of the half-metallic state in all of the theoretical approximations is a standard point of reference, making it a significant promise in terms of applications in the engineering of device builds. The calculated electronic structure shows that there is 100% spin polarization at the Fermi level, but this is based on an idealized ground-state scenario that doesn't consider spin-flip scattering mechanisms. In the real world, thermal excitations, spin–orbit coupling, and magnon scattering can cause transitions between spin channels, especially in systems with small minority-spin band gaps (about 0.143 eV). These kinds of things could cause effective spin polarisation to go down and spin-leakage currents to show up. So, even though the current results confirm intrinsic half-metallicity, temperature and relativistic effects may affect the actual spintronic performance. This means that more advanced methods that include SOC and finite-temperature transport phenomena need to be used to investigate this further.

The half-metallic behavior of Fe_2MnIn is a direct effect of orbital geometry, indicating that the orbital analysis of Fe_2MnIn indicated that DOS analysis revealed the behavior of the material. Figs. 5 and 6(a-e) show that both the Total and Partial Density of States are asymmetric with respect to spin. It is found that the majority-spin states span the Fermi level, while the minority-spin states are absent. Better treatment of the exchange-correlation energy results from transitioning from standard GGA to mBJ potential. An upward energy shift is applied to the conduction band Mn-3d states through the mitigation of self-interaction errors. This shift is the reason the minority-spin gap is augmented from 0.1 eV to 0.143 eV. A true physical property of the material is represented by the robust and confirmed half-metallic state. Fig. 6 indicates that the microscopic origin of the gap is due to the dominance of 3d orbitals from transition metals around E_F. Due to exchange-induced splitting, the Mn-3d majority states are deeply localized in the valence band, and the minority states are completely above the gap. Covalent-type interactions of t_2g and e_g orbitals on Fe and Mn sublattices result in the formation of the gap, as in Fig. 7.

Through the creation of a bonding-antibonding separation, E_F is isolated by site-specific d-d hybridization to ensure 100% spin polarization. The localization of In-p states is regarded as highly advantageous for device implementation. These states are shown by Fig. 6(d) and (e) to be deep valence features, hence not participating in conduction at E_F. Through the formation of an energy separation, p-d spin-flip scattering is minimized, preventing spin-current degradation [55]. Therefore, the electronic structure of inverse Fe_2MnIn advocates for its use in spin-transfer-torque (STT) devices. The provision of a decisive edge for ultra-low power switching is facilitated by near-perfect spin-torque efficiency.

3.5. Chemical bonding mechanisms

The chemical bonds and magnetic stability of the system are reflected in the distributions of spin-specific charge density illustrated in Fig. 7. According to the Pauling scale, the electronegativity values for the constituent elements are Iron (χFe = 1.83), Manganese (χMn = 1.55), and Indium (χIn = 1.78) [58]. Fe and Mn exhibit a minor $\Delta\chi$ of 0.28 in their electronegativities. Consequently, the low gradient across the lattice indicates a metallic-covalent hybridization bonding type. This is a characteristic feature in Heusler compounds that governs their electronic structure [59]. As shown in Fig. 7, the contour maps reveal directional bridges in the electron density, which proves that the d-d orbitals overlap considerably between transition metal sites. Because covalent hybridization allows for direct exchange interactions, it is a basic requirement for the material to sustain long-range ferromagnetic ordering [54,60].

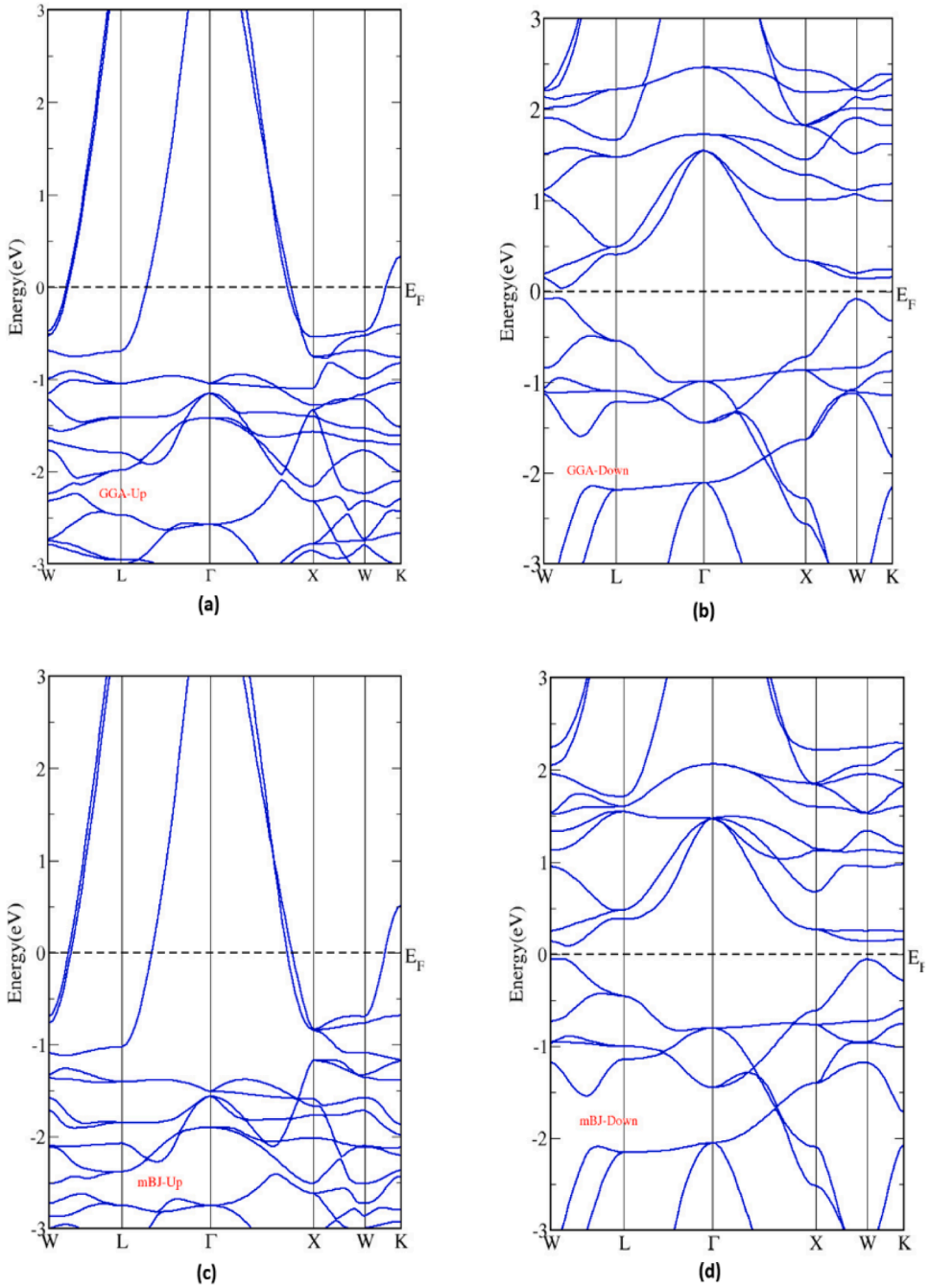

Fig. 4. Comparative band structures of Fe_2MnIn using GGA and mBJ functionals.

As evidenced by the lobe-shaped directional contours between Fe and Mn, there is a high degree of d-d covalent hybridization. Indium contributes to these alloys as an electron donor; consequently, its electron density appears as diffuse and spherical non-directional s-p contours [61]. Magnetic exchange coupling is operated by transition metals; the lattice, on the other hand, is maintained by the primary-group element through a homogeneous electronic background. These different bonding functions and roles are tabulated and summarized in Table 4. The high degree of similarity between the charge density contours of both spin channels in Fig. 8 suggests a strongly symmetrical structural construct for Fe_2MnIn. The primary determinants for the spatial redistribution of the total valence charge are the chemical potentials of the nuclei and the s-p metallic background of indium, rather than the d-orbital energy separation [62,63]. Even though d-orbital energy splitting is responsible for magnetic moments, it is not the mechanism that determines the spatial redistribution of the total valence charge. The regulating factors of this redistribution are the chemical potentials of nuclei and the s-p metallic background of Indium [64]. Considering that the electronegativity of Indium ($\chi = 1.78$) closely resembles that of Iron ($\chi = 0.05$), the Fe–In bond exhibits a significant degree of metallic delocalization (Table 4). Fig. 8 shows diffuse and spherically symmetric contours at the In sites; these act as a "metallic glue" to stabilize the $L2_1$ framework without affecting the magnetic d-bonding [65].

3.6. Optical properties

This study is a complete examination of the linear optoelectronic capabilities of Fe_2MnIn, capabilities assessed through the complex dielectric function ($\epsilon(\omega) = \epsilon_1(\omega) + i\epsilon_2(\omega)$) [66–68]. The capability of a

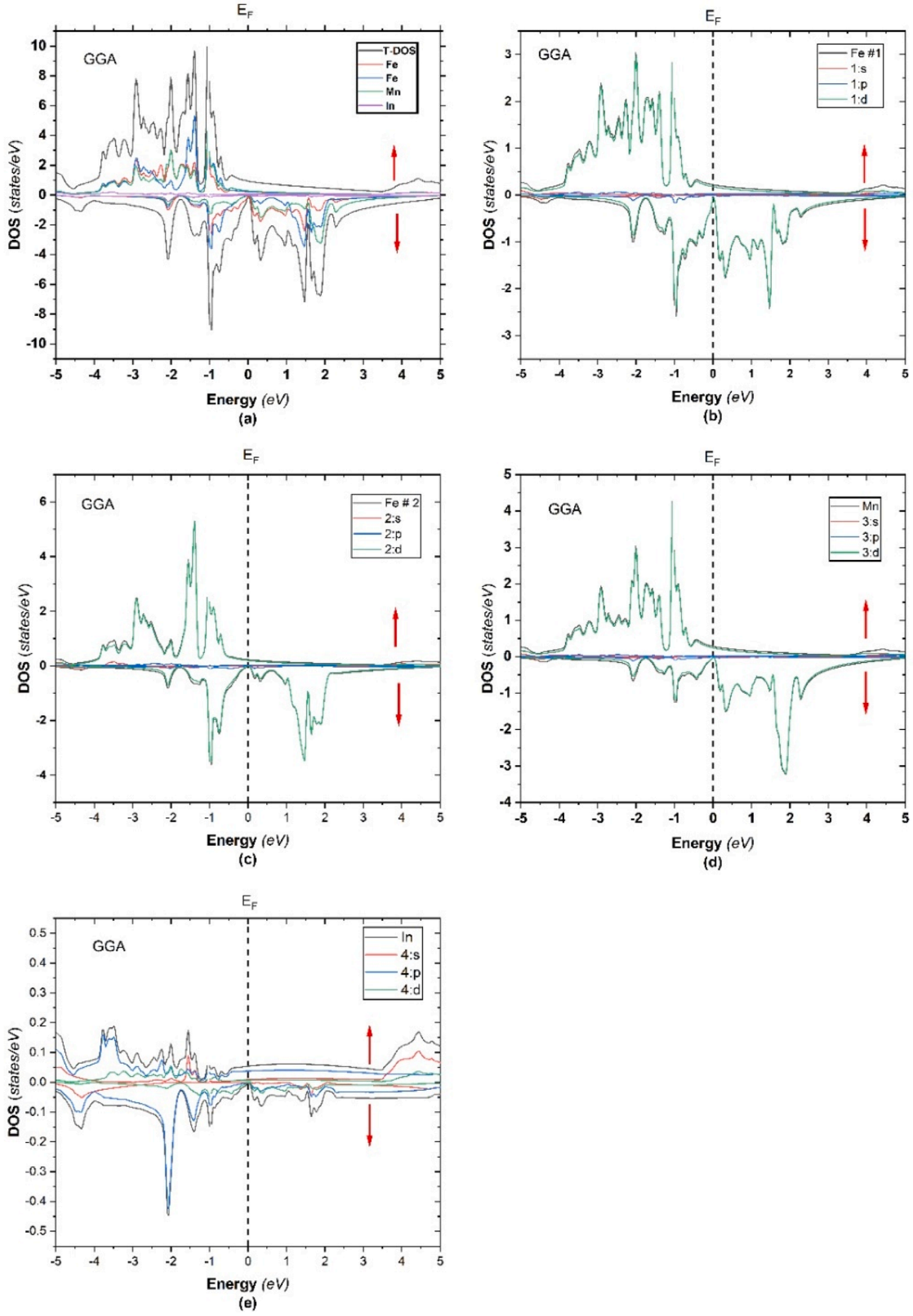

Fig. 5. Total and partial density of states for the Fe_2MnIn full-Heusler alloy (GGA).

dielectric to store energy is represented by $\epsilon_1(\omega)$. This real part is evaluated within the Kramers-Kronig framework.

$$\varepsilon_1(\omega) = \mathrm{Re}\ \varepsilon_{ij}(\omega) = \frac{2}{\pi} \boldsymbol{P} \int_0^{\infty} \frac{\omega' \,\mathrm{Im}\varepsilon_{ij}(\omega)}{\widehat{w}^2 - \omega'^2} d\omega' \tag{8}$$

The optical joint density of states is weighted by the momentum

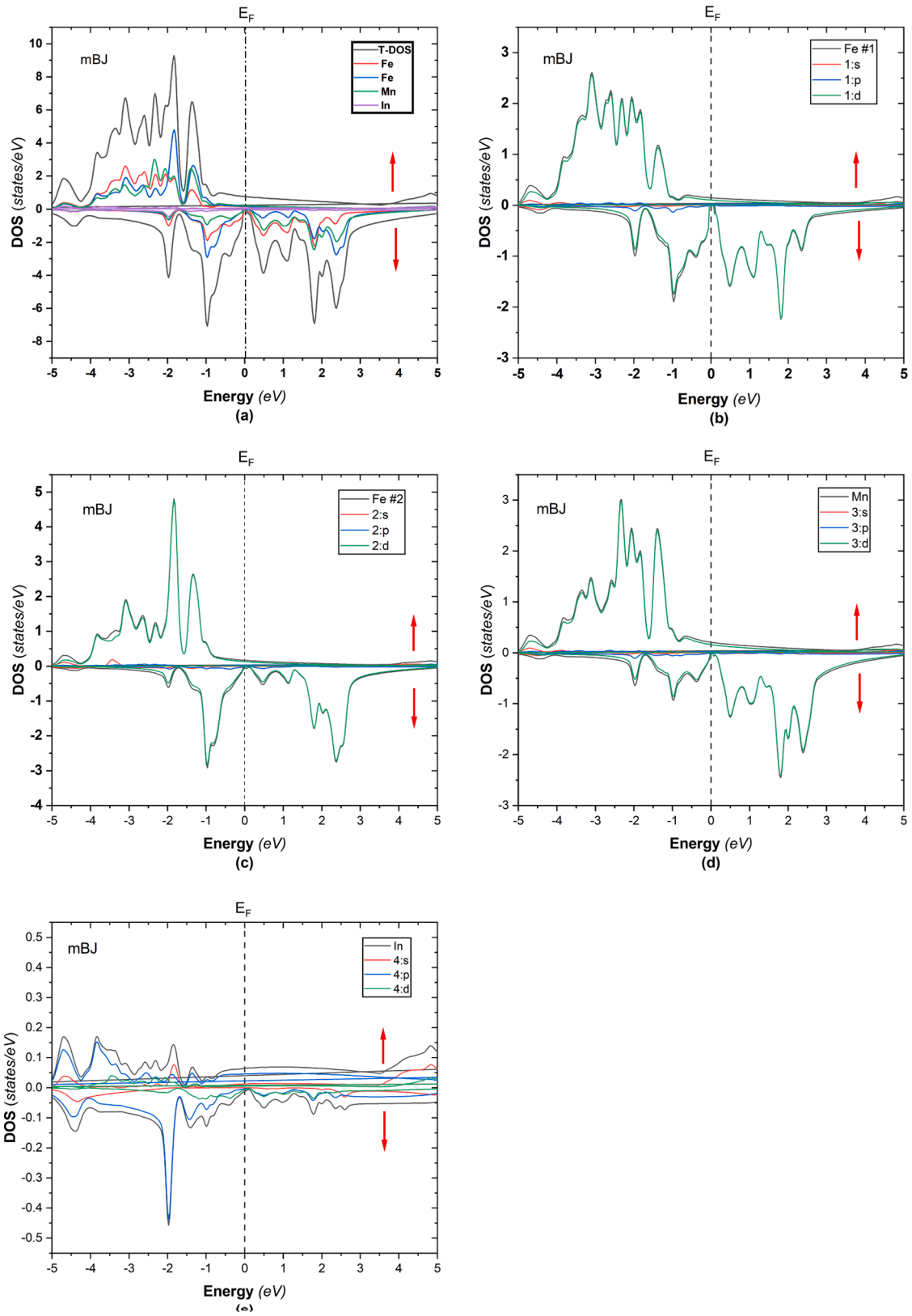

Fig. 6. Total and partial density of states for the Fe_2MnIn full-Heusler alloy (mBJ).

matrix elements of **P** to produce the physically observed $\epsilon_2(\omega)$ (Eq. 10).

$$\varepsilon_2(\omega) = \mathrm{Im}\varepsilon_{ij}(\omega)\frac{\hbar^2 e^2}{\pi m_e^2 \omega^2}\sum_{cn}\sum_{vn}\int dk \langle \Psi_k^{cn}|\mathrm{p}^i|\Psi_k^{vn}> < \Psi_k^{vn}|\mathbf{p}^j|\Psi_k^{cn}\rangle \sigma\left(E_k^{cn} - E_k^{n\nu} - \hbar\omega\right) \quad (9)$$

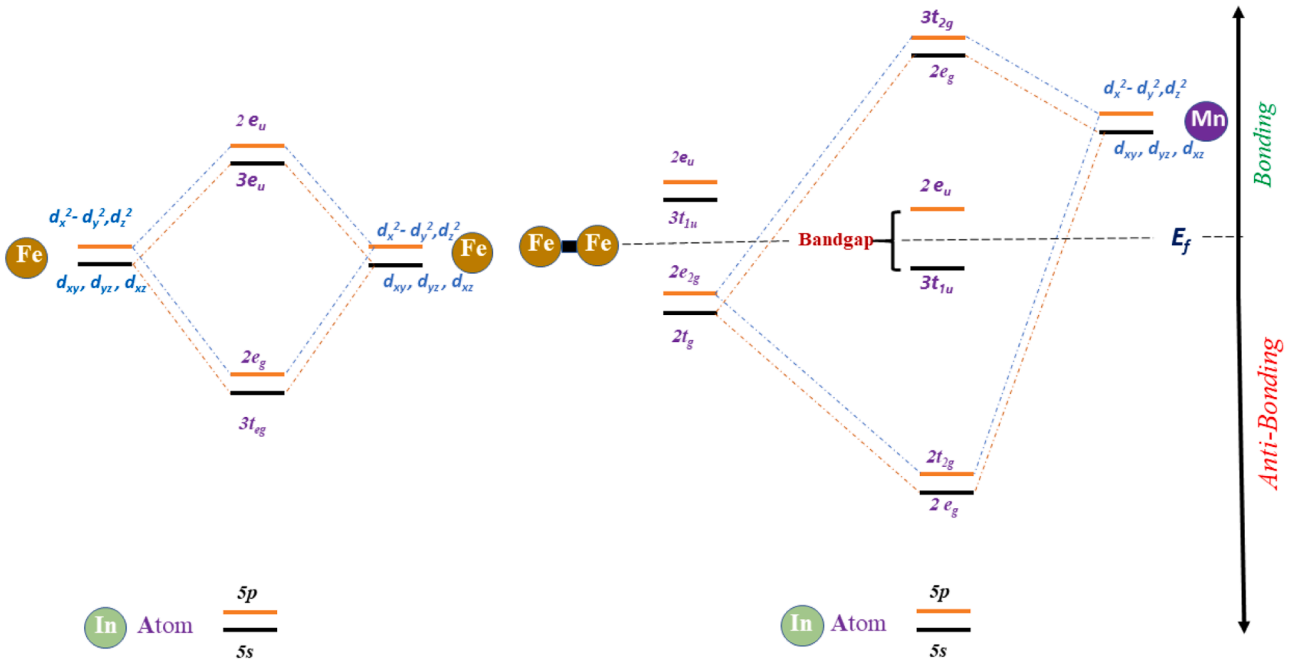

Fig. 7. Schematic of d-d orbital hybridization in Fe_2MnIn Heusler alloy.

Table 4
Charge density analysis of Heusler alloy.

Interaction	Δχ (Pauling)	Contour Shape	Bonding Nature
Fe–Mn	0.28	Directional Lobes	d-d Covalent Hybridization
Fe–In	0.05	Diffuse / Spherical	Metallic Delocalization
Mn–In	0.23	Diffuse / Spherical	p-d Metallic-Covalent

The superposition of two transition mechanisms (intra-band and inter-band) describes the optical signature of the half-metal Fe_2MnIn. The dispersive and absorptive qualities of the material are modeled using GGA and mBJ functionals and shown in Figs. 10–15. Optical properties reveal the electronic structure and band gap, which are the primary factors for developing photonic devices. Light absorption and reflection mechanisms are understood in detail when investigating the dielectric function, refractive index, extinction coefficient, and optical conductivity.

The $\varepsilon_1(\omega)$ curves for the spin-up state in Fig. 9(a) show that while GGA and mBJ methods are qualitatively similar, they differ quantitatively in the 0-8 eV range of the IR, visible, and UV regions. Specifically, the static dielectric constant is 103.4 according to GGA and 139.7 according to mBJ. There is a subsequent rise to a maximum between 0.2 and 0.3 eV, and the mBJ method yields a peak of 158.4. The effectiveness of screening electric fields induced by trapped charges in the low-frequency limit is represented by the value of the static dielectric constant [69]. After passing the peaks, the dielectric curves decline steeply until they cross the zero line at 0.75 eV (mBJ) and 0.88 eV (GGA). A negative excursion in the spectral decline reaches its minimum at 1.5 eV. Because the $\varepsilon_1(\omega)$ values at these minima reach -44.4 (GGA) and -40.8 (mBJ), they are symptomatic of free-carrier dominance. Both GGA and mBJ curves show a gradual return from their minima toward the zero threshold at 8 eV, attaining closely matched values of 0.9 and 0.8 [70, 71]. An earlier plasma frequency and smaller negative values are predicted by mBJ, when compared to GGA, suggests a better account of excitonic effects and lower free carrier screening.

The $\varepsilon_2(\omega)$ data for the majority spin in Fig. 9(b) was found to be in close agreement, establishing the absorption region's width. Energy dissipation and light absorption are the physical phenomena represented by the imaginary dielectric constant, which is mathematically related to the extinction coefficient. A qualitative assessment shows that the $\varepsilon_2(\omega)$ shapes for GGA and mBJ are varied, but their peak magnitudes show quantitative agreement at 163.94. The spectra begin with GGA $\varepsilon_2(w)$=1.03 and mBJ $\varepsilon_2(w)$=5.98 at 0.01 eV. The greatest peak value is the same for both approaches. The mBJ peak is blue-shifted by 0.16 eV

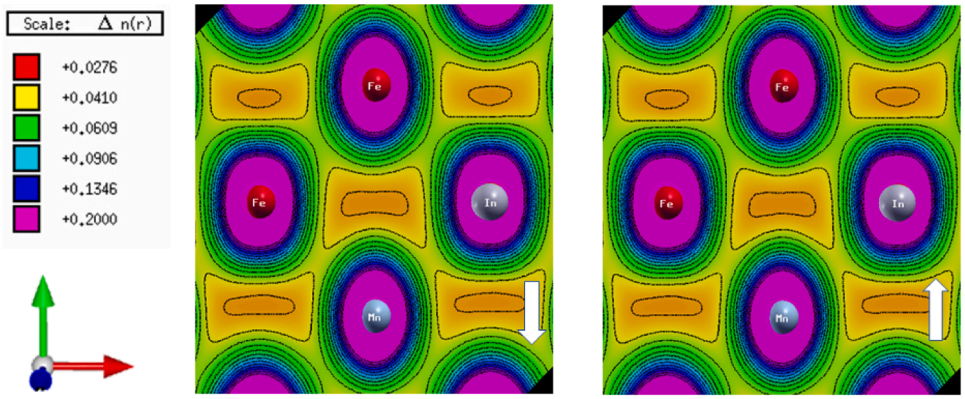

Fig. 8. Fe_2MnIn charge density distributions in the (110) plane.

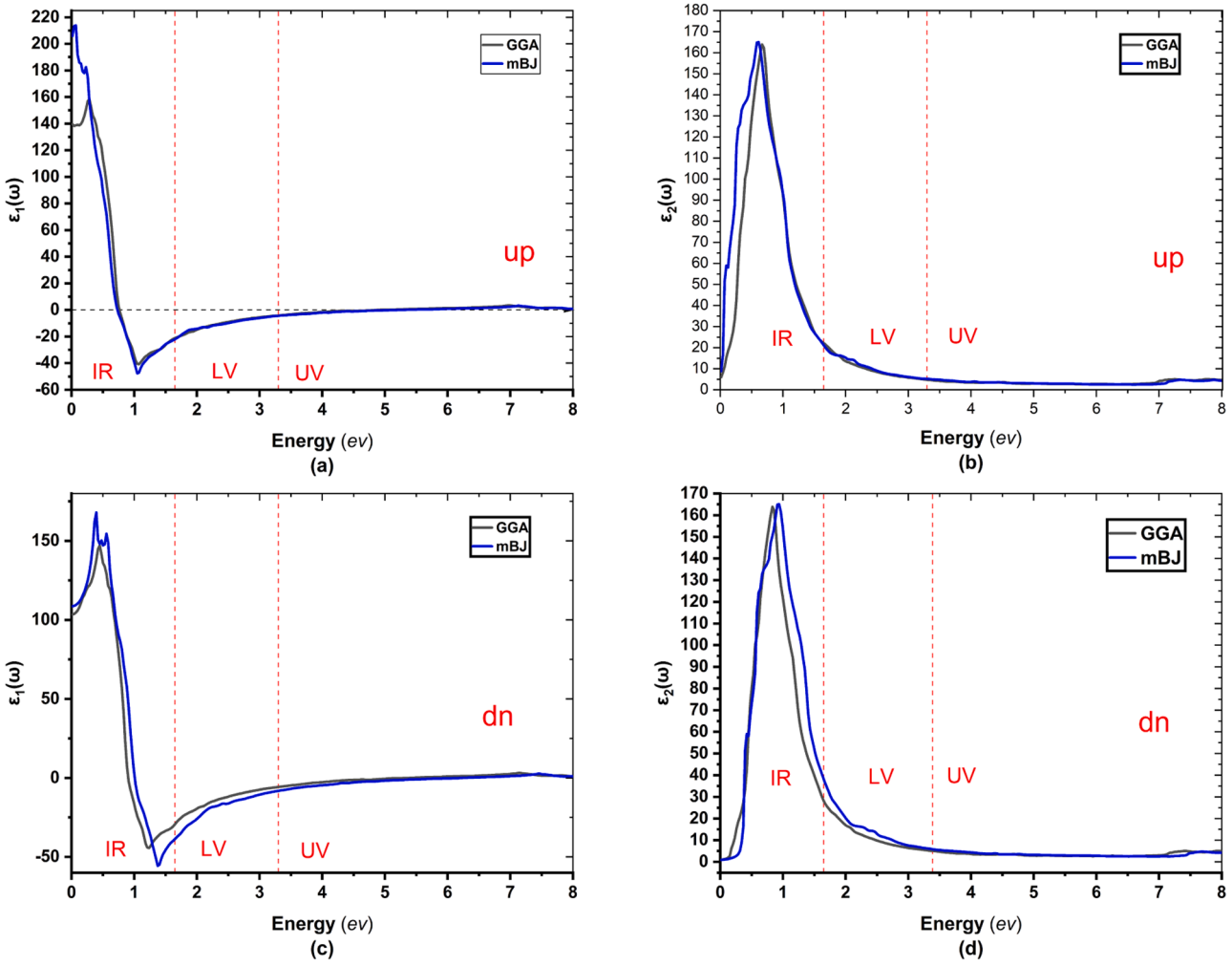

Fig. 9. Dielectric constant $\varepsilon_1(\omega)$ and primary $\varepsilon_1(\omega)$ peak for Fe_2MnIn, spin-up, GGA vs. mBJ.

compared to the GGA peak, occurring at 0.67 eV. The mBJ spectral curve indicates intense absorption and the presence of well-defined transition paths. It demonstrates a more precipitous increase and heightened low energy $\varepsilon_2(w)$. Following this, both the mBJ and GGA curves eventually experience rapid exponential decay and stabilize at values of 5 and 4.66, respectively. The mBJ functional provides a more accurate description of optical gaps; consequently, it predicts an earlier onset of absorption. However, the total absorption strength remains consistent with the GGA method.

Both the GGA and mBJ curves depicted in Fig. 9(c) for the spin-down manifest high starting points. While the GGA plot begins at 103.4 and peaks at 148.4, the mBJ plot starts at 105.6 and achieves a much higher peak of 168.1. Beyond their peak positions, the two curves exhibit rapid downward trends and cross zero at closely matching energies of 0.91 eV in GGA and 1.02 eV in mBJ, indicating comparable plasma frequencies in the spin-down channel. The curves thereafter experience a negative deviation, with mBJ attaining a minimum of -55.58 and GGA reaching -44.01. The mBJ functional demonstrates a more distinct metallic nature than GGA, but the curves ultimately converge to the same baseline value.

The radiation absorption of the compound is captured by the $\varepsilon_2(\omega)$ curve in Fig. 9(d). This specific component regulates the dissipation of energy and the optical absorption spectrum through interband transitions of electrons. Comparable peak intensities characterize the spin-down channel of the imaginary dielectric function $\varepsilon2(\omega)$. Subtle disparities nevertheless exist in the optical spectrum's defining parameters for energies from 0 to 8 eV. The parameters of exact peak energy and asymmetric broadening shape show these disparities, which are suggestive of important selection rules that depend on spin. Optical absorption starts once the photon energy crosses the band gap, and $\varepsilon2(\omega)$ is zero before this point. It is evident from the 0.06 eV blueshift that mBJ enhances excitonic binding, with peak values recorded at 165.07 and 163.94 respectively. The mBJ spectrum shows the initial rise is sharper and has a higher baseline, indicating that it has better absorption at low energy in comparison to GGA, implying a higher concentration of oscillator strength. Following peak values, both curves decrease at a rapid exponential rate, reaching 4.66 for GGA and 4.35 for mBJ at 8 eV. As shown by the properties of the spin-down spectrum, mBJ provides a more accurate prediction of spin-polarized critical points and excitonic resonances. It is anticipated that the leading absorption edge will be observed at the lower photon energy, without loss of peak intensity.

The phase velocity of light is determined by the absorption spectrum over all frequencies because the real and imaginary refractive index components are connected. To arrive at a deduction of these properties, the scientific community adopts the logical links generated in the upcoming mathematical representations:

$$\mathrm{n}(\omega) = \left[\frac{\sqrt{(\epsilon_1^2(\omega) + \epsilon_2^2(\omega)} + \epsilon_1(\omega)}{2}\right]^{\frac{1}{2}} \tag{10}$$

$$\mathrm{k}(\omega) = \left[\frac{\sqrt{(\epsilon_1^2(\omega) + \epsilon_2^2(\omega)} - \epsilon_1(\omega)}{2}\right]^{\frac{1}{2}} \tag{11}$$

The refractive index n(ω) and extinction coefficient κ(ω) of Fe_2MnIn for spin-up and spin-down electrons are illustrated in Fig. 10. Fig. 10(a) and (b) show the majority spin results, while Fig. 10(c) and (d) show the minority spin results, calculated using GGA and mBJ. The complex refractive index determines the light propagation and light absorption in a material, with its elements being n(ω) and k(ω). In particular, n(ω) is the phase velocity of light, and k(ω) is the degree of strength of absorption. The relationship between n(ω) and $\varepsilon_1(\omega)$, the real part of the dielectric function, given by $n(0) = \sqrt{(\varepsilon_1\ (0))}$ [72], is confirmed by the calculated static refractive indices. Owing to the sharp growth in the spin-down refractive index n(ω) and extinction coefficient n(ω), the occurrence of pronounced magneto-optical effects is substantiated. Substantially higher values of the refractive index at ω = 0 eV characterize the spin-up electrons. The results depicted in Fig. 9 show that the spin-up state possesses values of 11.82 for GGA and 14.35 for mBJ, which contrast with the diminished spin-down values of 10.17 and 10.42. The mBJ spin-up results are significant because they show a 38% increase at the static limit, followed by a peak of 14.73 at the low energy of 0.07 eV. The dependence of the refractive index on carrier spin polarization is shown to be highly pronounced in this system. The refractive index drops sharply for both functionals; consequently, the minimum is observed to occur between 3.5 and 3.9 eV. Spin asymmetry is shown in the complementary features of the extinction coefficient K (w). The onset values at low energy are 0.25 for GGA and 0.31 for mBJ. Compared to the spin-down magnitudes, these spin-up results are five to seven times greater. The resonance energies of 0.88 eV and 1.35 eV are obtained because of the 0.16 eV and 0.33 eV spectral shifts in GGA and mBJ. This signifies that spin-orbit coupling is more pronounced and the bands are modified. The values for n(w) and k(w) stabilize at 1.6 and 1.3 to 1.4 at 8 eV, irrespective of spin channel or functional. The convergence depicts the physical idea that spin-dependent changes in the band structure that provide significantly enhanced low-energy optics of spin-down electrons do not influence the common joint density of states that defines the high-energy optical absorption and dispersion.

The plots in panel (d) of Fig. 10 show that the extinction coefficient and the loss component of the dielectric function, $\varepsilon_2(\omega)$, are zero over identical low-energy ranges ($\hbar\omega < E_{gap}$), maintaining a value of zero until the band gap energy is reached. The calculated absorption shows

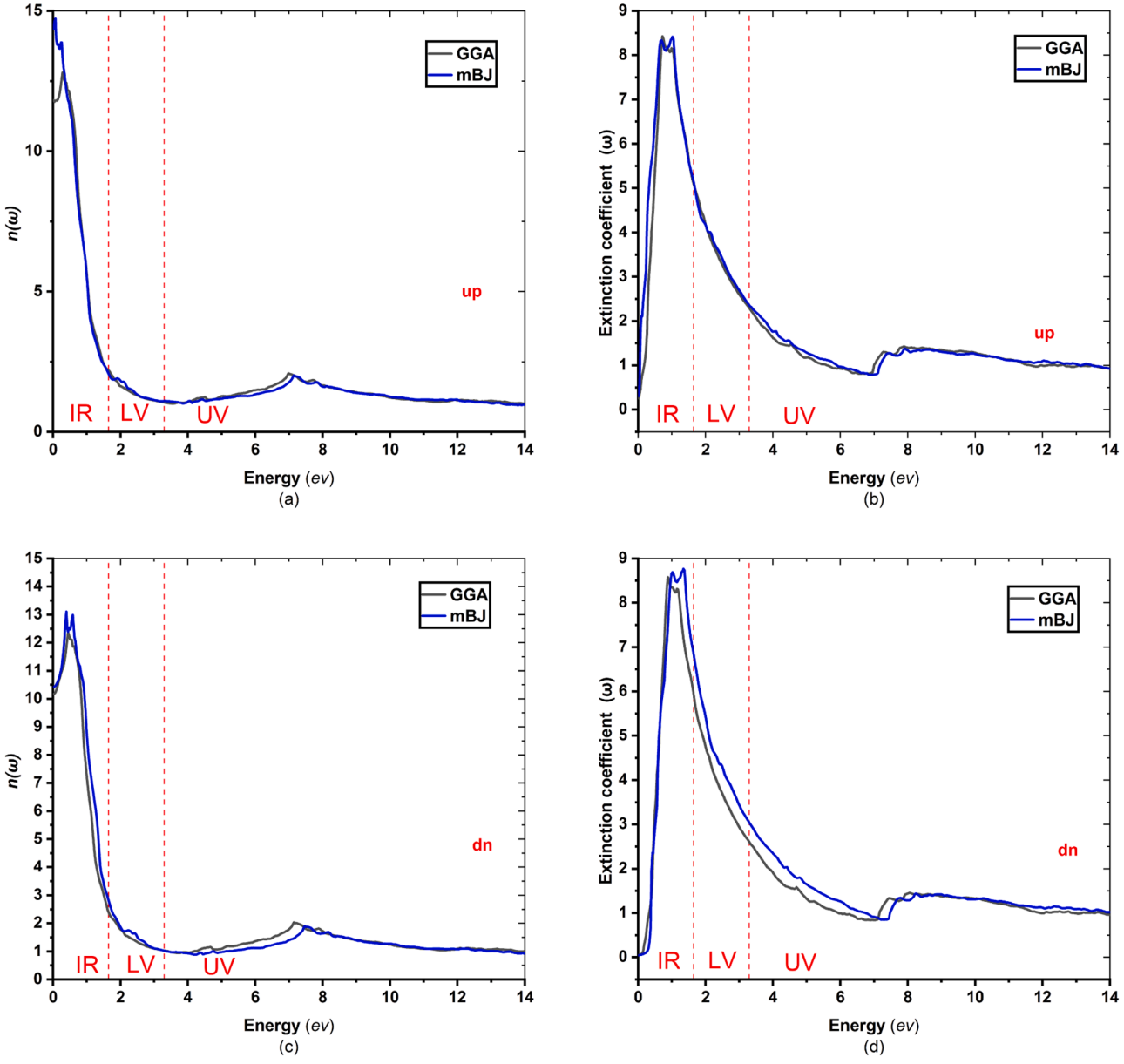

Fig. 10. The refractive index n(ω) and extinction coefficient κ(ω): spin-up and spin-down channels, GGA vs. mBJ.

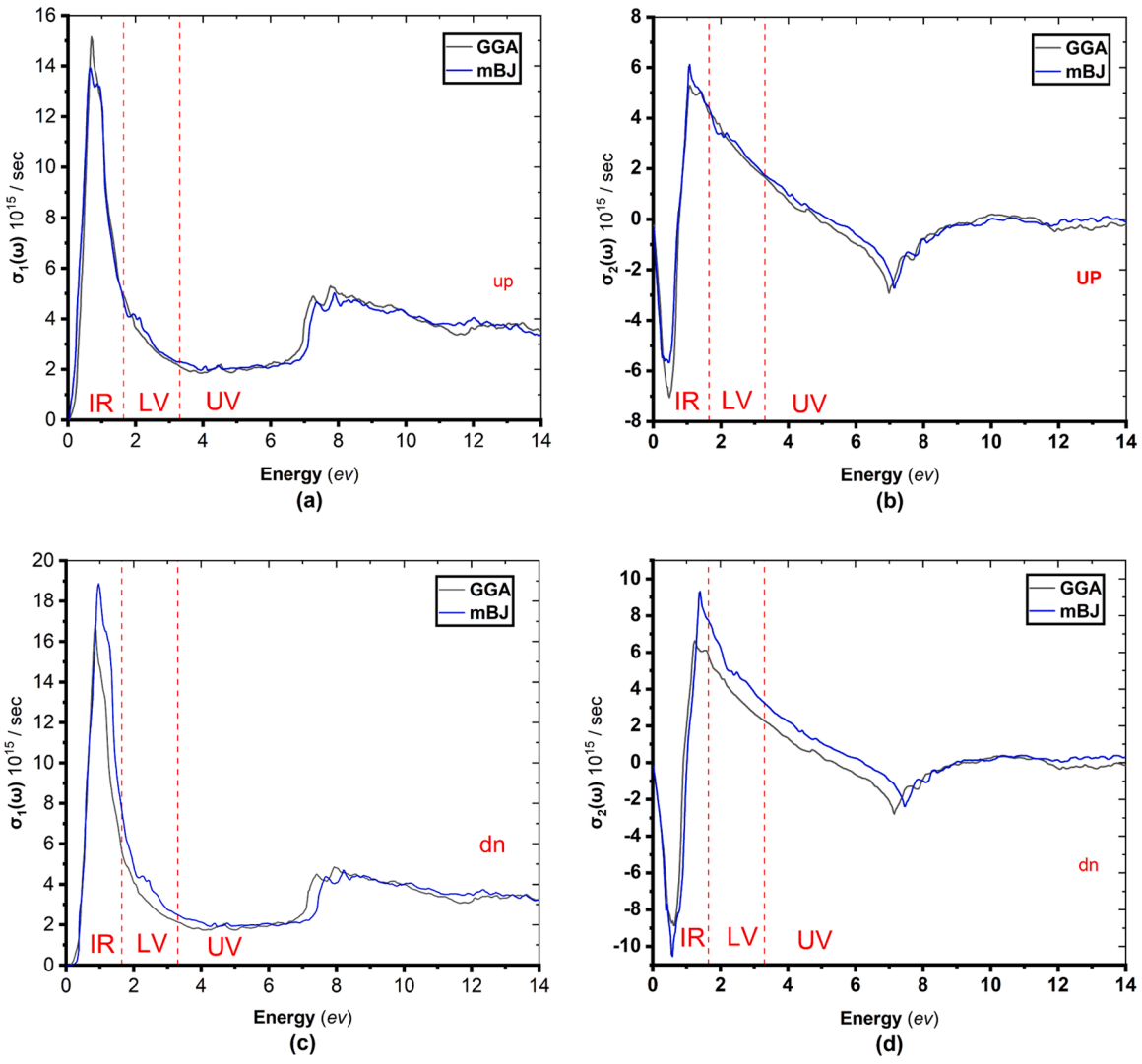

Fig. 11. The complex optical conductivity for spin-up channel, GGA vs. mBJ.

that peaks develop immediately above the band gap. The mBJ approach produces peaks of increased magnitude and shifts them toward higher energies compared with GGA. The spectroscopic data shows the first peak migrating from 0.88 eV to 1.35 eV (ΔE=0.47 eV) and increasing in intensity from 8.58 to 8.77. These observations prove that functional selection is critical only for low-energy features, as the high-energy response is functionally invariant. The mBJ approach is, for this reason, especially significant for achieving precision in low-energy properties such as excitonic effects and optical gaps in magnetic materials.

Therefore, this study is essential for the accurate simulation of spin-variant magneto-optical interactions and the strategic design of spintronic photonic devices. Waveguide propagation, interfacial reflection and transmission, and cavity resonance are predominantly influenced by the refractive index of the material. Due to the dispersion levels in Fe_2MnIn, it is a premier candidate material for UV detection and wavelength filtration. The spin-sensitivity of the optical response is essential for advancing polarization-modulated spintronics. A comprehensive understanding of these processes enables the advancement of opto-electronic devices.

The electrical conduction of a material in response to light's oscillating field is defined by Equation (12) as complex optical conductivity, including dissipative and reactive parts [73].

$$\sigma(\omega) = \sigma_1(\omega) + i\sigma_2(\omega) = -i\varepsilon_0\omega(\varepsilon(\omega) - 1) \quad (12)$$

This paper reports on the complex optical conductivity $\sigma(\omega) = \sigma_1(\omega) + i\sigma_2(\omega)$. While light intensity decay is linked to the real part $\sigma_1(\omega)$, the phase change of the electromagnetic wave is linked to the imaginary part $\sigma_2(\omega)$ [73–75]. Within the range of 0 to 2 eV, the $\sigma_1(\omega)$ spectra display sharp peaks of significant height, which is a clear indication of major interband transitions. Maxima for absorption are at 0.67 eV and 0.97 eV for mBJ and GGA. Further absorption is detected throughout the visible light region (1.8–3.1 eV) and above 6 eV. Because of the observed high-intensity absorption characteristics, this substance appears to be an excellent prospect for the development of high-efficiency photodetectors. Changes in the signs of $\sigma_2(\omega)$ also give useful information about the dielectric function and the photon energies at which the material most effectively stores electromagnetic energy by means of induced polarization, which is a key characteristic of the material's frequency-dependent complex permittivity [76]. From the plots of the real conductivity $\sigma_1(\omega)$, the behavior of the individual spin channels with respect to charge transport is inferred from the DC conductivity value and the energy of its onset. The improved conductivity at 0 eV and pronounced $\sigma_1(\omega)$ peaks in the infrared spectrum for the spin-up orientation indicate that the channel exhibits metallic characteristics [77]. This observation refutes the potential classification of the material as a half-metal or a semiconductor. The lack of a zero-conductivity threshold in $\sigma_1(\omega)$ for both spin orientations prior to absorption indicates that the spin-down channel lacks a semiconducting gap. Its immediate

conductivity onset from low photon energy is incompatible with a gapped electronic structure for this channel [78]. Changes in the magnitude and energy of transitions are evident when different computational methods are used to study the optical response. A side-by-side spectral comparison confirms the tendency of the Generalized Gradient Approximation (GGA) to overestimate the values of the real conductivity. Mean optical conductivity is boosted by 4.8 percent and peak response by 34 percent using the GGA method. The peak transition energies are shifted to 0.67–0.69 eV by the mBJ functional, which is an improvement over the GGA range of 0.86–0.97 eV because the mBJ functional is better at predicting the band gap and thus more accurate for electronic transitions. Furthermore, the use of mBJ leads to a significant strengthening of the $\sigma_2(\omega)$ spectrum (by 10–28%) and an eightfold improvement in the correctness of spin polarization. Regarding high-performance optoelectronics, the requirements are satisfied by the high values predicted by the GGA functional, which provide a 25–38% benefit in the visible spectrum. High spin polarization accuracy, as predicted by the mBJ functional, is pertinent to spin injection and thus addresses the requirements for efficient spintronics [79, 80].

The optical reflectivity $R_{ij}(\omega)$ of FeMnScGa is calculated from the complex dielectric function using Equation (13) [73]:

$$R_{ij}(\omega) = \left[\frac{(\mathrm{Re}\varepsilon_{ij} + \mathrm{iIm}\varepsilon_{ij})^2 - 1}{(\mathrm{Re}\varepsilon_{ij} + \mathrm{iIm}\varepsilon_{ij})^2 + 1}\right] \tag{13}$$

As shown in Fig. 12, the reflectivity spectra for Fe_2MnI have been calculated for both spin-up and spin-down states using both the GGA and mBJ methodologies. In Fig. 12(a), which shows the spin-down channel, the static reflectivity is around 59% with GGA and 65% with mBJ. The reflectivity is found to peak at 71% for GGA and 80% for mBJ in the infrared, then decreases gradually and oscillates before reaching a steady 40% to 55% throughout the visible and ultraviolet areas. At low energy, the metallic nature of the compound is indicated, whereas interband electronic transitions gain more role at higher photon energy. The behavior of the dielectric function is directly, causally, related to the oscillatory reflectivity, where the nature of the dielectric function is dependent upon the determinants of the band structure. Regarding the spin-up channel shown in Fig. 12(b), the static reflectivity is calculated at 75% for GGA and 72% for mBJ, with both functionals reaching a peak reflectivity of about 80% in the infrared region. The high reflectivity level in the infrared spectral region is a direct measure of the high metallic conductivity, and the successive decrease in the reflectivity extending to the ultraviolet region is a measure of the increased optical absorption due to interband electronic excitation. It is evident that reflectivity shares an inverse relationship with absorption and conductivity, meaning that the weakening of reflection leads to the strengthening of absorption and optical transport. The findings as a whole indicate that the spin-dependent reflectivity of Fe_2MnIn is distinct for both spin-up and spin-down channels. These results, in light of the absorption and conductivity data, suggest the material's potential in spintronic and magneto-optical devices like spin filters [81–83].

The absorption coefficient $\alpha(\omega)$ arises from the analysis of both the real and imaginary parts of the complex dielectric function [84]:

$$\alpha(\omega) = \frac{\sqrt{2}\,\omega}{c}\sqrt{-\varepsilon_1(\omega) + \sqrt{\varepsilon_1(\omega)^2 + \varepsilon_2(\omega)^2}} \tag{14}$$

Fig. 13a and b of typical low-energy behavior in *Fe_2MnIn* by absorption spectroscopy give the definitive optical evidence of its half-metallic ferromagnetism, which is based on spin-channel-dependent electronic bands. The metallic and semiconducting duality of the two spin channels in a ferromagnetism material ensures that the optical absorption onset for each channel is a direct representation of the corresponding band gap E_g. The spin-up channel absorption spectra (Fig. 13a) indicates that magnitude between $85 \times 10^4\ cm^{-1}$ and $100 \times 10^4\ cm^{-1}$ are reached starting at 0 eV. Strong absorption that begins suddenly in the optical spectra indicates the metallic character of the material. In the low-energy region, the absorption values for the semiconducting spin-down channel (Fig. 13b) are quantitatively larger than those of the spin-up channel, reaching an intensity of ~120 units in GGA. A sharp decrease in the curve is localized at the 2-6 eV range, where it hits a minimum. This is immediately succeeded by a notable gain in higher energy. Standard semiconductor behavior is contradicted by two factors: the occurrence of sub-gap absorption and the 20-30-unit elevation of the spin-down channel intensity. Low-energy optical transitions are made possible for valence electrons by the proximity of states to the Fermi level, as suggested by this experimental deviation. Rapid absorption decrease to the minimum is characteristic of a spin-down semiconducting gap, underestimated by GGA. Spin-dependent onset, peak, and decay of absorption spectra indicate the half-metallic nature of the material. That Fe_2MnIn possesses discrete metallic and semiconducting spin channels is confirmed by our findings. High spintronic potential is indicated by the theoretical 100% spin polarization of charge transport at the Fermi energy.

L(w) is the key variable for calculating the energy loss probability of a fast-charged particle in all forms of materials.

$$L_{ij}(\omega) = -\mathrm{Im}\left\{\frac{1}{\varepsilon_{ij}(\omega)}\right\} = \frac{\mathrm{Im}\varepsilon_{ij}}{(\mathrm{Re}\varepsilon_{ij})^2 + (\mathrm{Im}_{ij})^2} \tag{15}$$

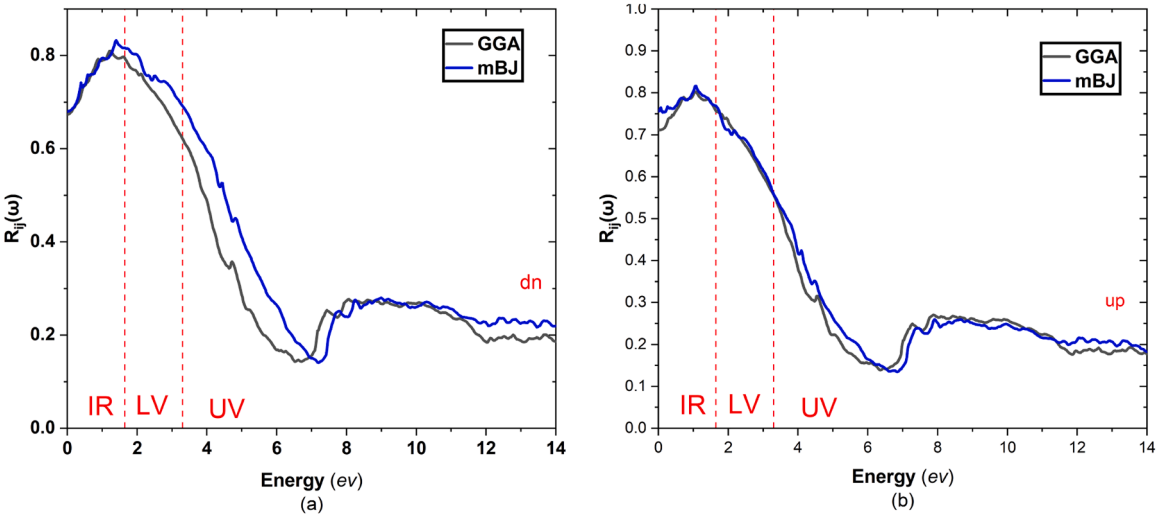

Fig. 12. The optical reflectivity $R_{ij}(\omega$ for both spin channels, GGA vs. mBJ.

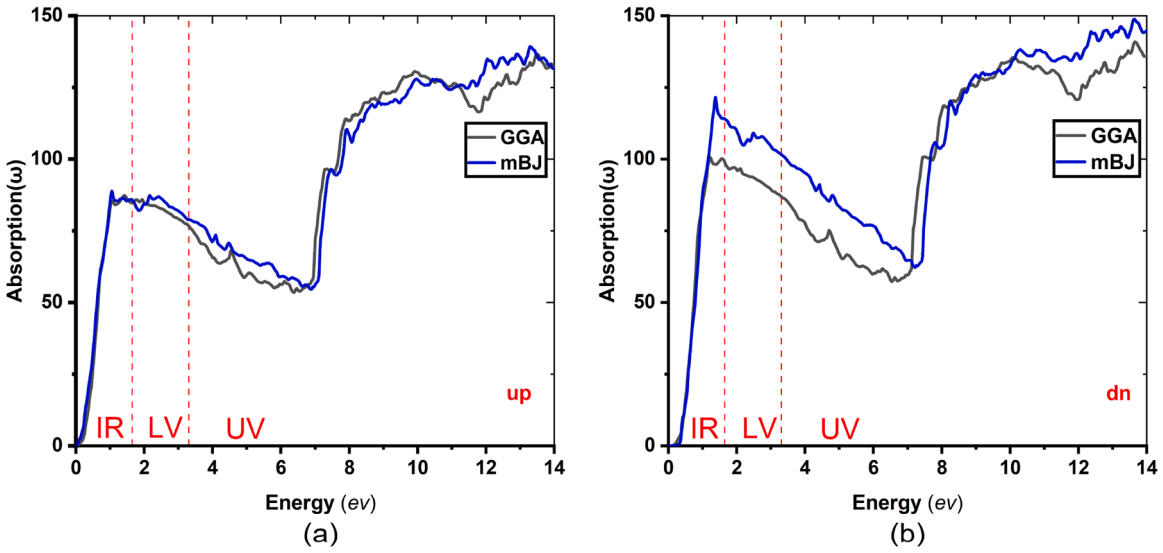

Fig. 13. Absorption coefficient α(ω) in 10^4 cm^{-1} for up-spin channel, GGA vs. mBJ.

The spin-polarized electronic structure of Fe_2MnIn, a half-metal, is directly verifiable through the study of its theoretically obtained electron energy loss optical spectra. That electronic states are highly sensitive to the exchange-correlation functional is a conclusion supported by the electron energy loss optical spectrum, L(ω). The down-spin channel, depicted in Fig. 14(b), exhibits smaller functional variations than the up-spin channel, even though mBJ increases the peak from 5.293 eV to 5.891 eV. It is found that mBJ increases optical transition energies by establishing a wider band gap than the standard GGA functional. The up-spin spectra obtained with mBJ, shown in Fig. 14(a), show clear and accurate depiction of the minority electronic states. The mBJ approach causes the main peak to shift to 6.245 eV from the GGA energy of 5.483 eV and to narrow, as reflected in the reduction of FWHM from 3.973 eV to 3.347 eV. Provided a difference analysis is conducted, mBJ is further confirmed by the positive +0.151 at 7.14 eV in the up-spin channel compared to GGA. The GGA functional underestimates high-energy d-d transition energies. These transitions are identified as the most significant mechanisms for the control of Fe_2MnIn's physical nature. The material Fe_2MnI is proven effective for spintronic systems by the evidence of pronounced spin-dependent optical activity. A summary of these optical properties and their comparison between GGA and mBJ is presented in Table 5.

We used the modified Becke–Johnson (mBJ) potential to calculate the optical properties of the studied system within the independent particle approximation (IPA). This potential gives a better picture of the electronic band structure and optical transitions than standard DFT functionals. This method does a good job of showing the main parts of the dielectric response, but it doesn't include many-body effects like excitons, which are interactions between electrons and holes. In spin-polarized and half-metallic systems, excitonic effects can significantly influence oscillator strength redistribution, absorption edge modification, and peak intensity alteration. So, the calculated absorption spectra and dielectric functions should be seen as showing how a single particle reacts to light. Nonetheless, the general spectral trends and relative comparisons continue to be qualitatively dependable within this context. The Bethe–Salpeter Equation and Time-Dependent Density Functional Theory are two advanced methods that could give a more accurate picture of excitonic contributions. These methods are not part of this study, but they are important areas for future research.

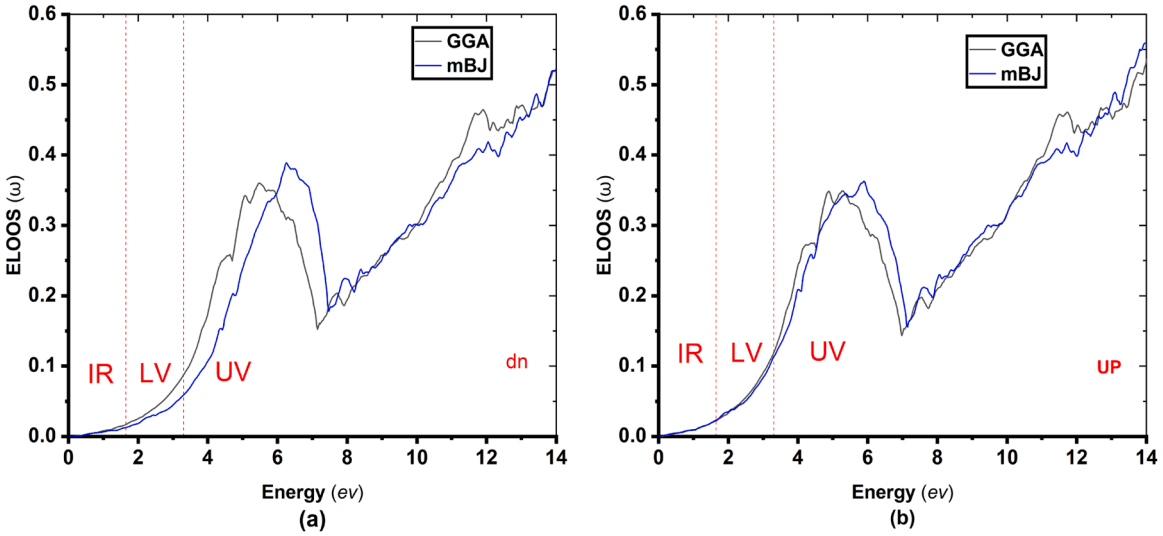

Fig. 14. EELOS difference (mBJ–GGA) for up-spin channel, highlighting high-energy d–d transition enhancement.

Table 5
Optical and electronic properties of Fe_2MnI comparing GGA and mBJ.

Property	Spin channel	GGA Result (Units/ Energy)	mBJ Result (Units/ Energy)	mBJ/GGA Comparison & significance	Reference figure
Static Dielectric Constant ($\varepsilon_1(\omega)$ at 0.01 eV)	Spin-up	103.4	139.7	mBJ is 35.1% higher, predicting a stronger low-energy dielectric response.	1(a)
Primary $\varepsilon_1(\omega)$ Peak Maximum	Spin-up	147.1	158.4	mBJ is 7.6% higher and sharper.	1(a)
Primary $\varepsilon_2(\omega)$ Peak Maximum	Spin-up	163.94 at 0.83 eV	163.94 at 0.67 eV	Identical magnitude, but mBJ is 0.16 eV blueshifted, indicating an earlier strong optical transition.	1(b)
Primary $\varepsilon_2(\omega)$ Peak Maximum	Spin-down	163.94 at 0.67 eV	165.07 at 0.61 eV	mBJ is slightly higher and 0.06 eV blueshifted, suggesting enhanced excitonic binding.	1(d)
Static Refractive Index (n(ω) at 0 eV)	Spin-up	11.82	14.35	mBJ shows 21.4% enhancement, indicating exceptionally strong spin-dependent refractive response.	2(a)
Primary Extinction Coefficient (κ(ω)) Peak	Spin-up	8.58 at 0.88 eV	8.77 at 1.35 eV	mBJ is 0.47 eV shifted to higher energy (blueshift) and slightly higher in magnitude, improving optical gap prediction.	2(d)
Real Conductivity ($\sigma_1(\omega)$) Peak Energy	Both	0.86–0.97 eV	0.67–0.69 eV	mBJ provides a downward shift in transition energy, offering a more accurate estimate of electronic transition energies.	3(a), 3(c)
Maximum EELOS Peak Energy	Up-spin	5.483 eV	6.245 eV	mBJ shifts peak 0.762 eV higher and narrows FWHM, indicating better band gap and spectral resolution.	6(b)
EELOS Difference (mBJ–GGA)	Up-spin	N/A	+0.151 at 7.14 eV	GGA significantly underestimates high-energy d–d transitions by 0.151 units.	6(b)
$\sigma_1(\omega)$ Conductivity Magnitude	Both	Up to 34% higher peak	Lower	GGA overestimates magnitude; mBJ predicts better maximum optical performance (e.g., 25–38% improvement for LEDs).	3(a), 3(c)
Spin Polarization	Inferred	Lower	8 × better prediction	mBJ is the superior method for spintronic applications due to enhanced spin polarization.	N/A

3.7. Thermodynamic properties

The Heusler compound Fe_2MnIn is subjected to thermodynamic analysis over 0–1000 K to acquire fundamental knowledge about its stable existence and characteristic atomic vibrations. This study employs the quasi-harmonic Debye framework [85].

$$S(T) = k_B\left\{\int\left\{\frac{\hbar\omega}{k_{BT}}\right\}\{\exp(\hbar\omega/k_BT)-1\}^{-1}F(\omega)d\omega - \int F(\omega)\ln[1-\exp(-\hbar\omega/k_BT)]d\omega\right\} \quad (16)$$

$$C_V(T) = k_B\int\left\{(\hbar\omega/k_BT)^2\exp(\hbar\omega/k_BT)\right\}\left\{[\exp(\hbar\omega/k_BT)-1]^2\right\}^{-1}F(\omega)d\omega \quad (17)$$

$$E(T) = E_{(tot)} + E_{(zp)} + \int\frac{\hbar\omega}{\exp(\hbar\omega/k_BT)}F(\omega)d(\omega) \quad (18)$$

$$F(T) = E_{(tot)} + E_{(zp)} + k_BT\int F(\omega)\ln[1-\exp(-\hbar\omega/k_BT)]d(\omega) \quad (19)$$

Complex lattices are indicated by the results of calculations for the thermodynamic parameters entropy (*S*), constant-volume heat capacity (*Cv*), internal energy (*U*), and Helmholtz free energy (*F*). Illustrating the findings at cryogenic and high temperatures, the specific values for these parameters are listed in Table 6. Fig. 15(a-b) shows the temperature-dependent vibrational thermodynamic characteristics of the substance computed between 0 K and 1000 K, as per phonon density of states.

The results in Fig. 15a indicate that the constant volume heat capacity *Cv* of Fe_2MnIn increases rapidly at low temperatures and reaches 0.071 *J/mol·K* at 5 K. Evidence of the gradual excitation of long-wavelength acoustic phonons is seen in this trend, as it follows the Debye T^3 law. The Cv curve approaches an asymptotic limit of 24.73 *J/mol·K* when the temperature progresses to 1000 K. Because the value is so close to the $3R \approx 24.9$ *J/mol·K* limit, it is evident that the vibrational degrees of freedom in Fe_2MnIn are almost fully populated [86].

Table 6
Theoretical vibrational parameters of Fe_2MnIn at low and high-temperature limits.

Parameter	T=5 K	T=1000 K
Heat Capacity (Cv)	0.0710 J/mol·K	24.73 J/mol·K (~3R)
Entropy (S)	0.0574 J/mol·K	57.76 J/mol·K
Free Energy (F)	~3.740 kJ/mol	−32.61 kJ/mol
Internal Energy (U)	3.74 kJ/mol	25.15 kJ/mol

Both the phase stability and thermal attributes of the material are further defined by the energy and entropy S trends presented in Fig.s 15a and b. Entropy increases from 0.0574 *J/mol·K* to 57.76 *J/mol·K* over the temperature range 5–1000 K as optical phonons of high frequency become progressively excited. According to thermodynamic principles, the internal energy (*U*) has to increase with temperature as a result of the introduction of vibrational energy to the system because $dU/dT = Cv > 0$. On the other hand, the Helmholtz free energy (*F*) should decrease with the rise in the entropy, and according to the law, $dF/dT = -S < 0$.

The absorption of heat causes the internal energy (U) to increase and (F) to decrease from 3.7405 kJ/mol to -32.61 kJ/mol at 1000 K, as shown in Fig. 15b. The deviation is consistent with the basic law of thermodynamics expressed as F = U - TS. The growing preponderance of the -TS component at high temperatures is a standard feature of equilibrium crystalline structures [87].

The value of 3.74 kJ/mol for the Zero-Point Energy of Fe_2MnIn is a major finding that informs the rest of this analysis. This energy is the quantum mechanical ground-state vibrational energy that is an inalienable property of the system at absolute zero. With a cryogenic temperature of 5 K, the internal energy (3.7408 kJ/mol) and free energy are almost equal since the thermal contribution (*TS*) is negligible. This establishes the fact that at low temperatures the energetics of Fe_2MnIn are dominated virtually exclusively by vibrational motion of the ground state of the atoms of Fe, Mn, and In in the lattice.

3.8. Dynamical Stability

To calculate the phonon dispersion curve, which is necessary to confirm the dynamical stability of the given compound, quantum ESPRESSO was used to calculate the linear response calculations [46]. The dynamical stability of the Fe_2MnIn Heusler alloy is confirmed by its phonon dispersion spectra, which show that all vibrational branches across the high-symmetry paths maintain real and positive frequencies (see Fig. 16). Because imaginary modes are entirely absent, we can conclude that the $L2_1$ cubic structure sits at a genuine local energy minimum; this ensures the lattice won't undergo any spontaneous

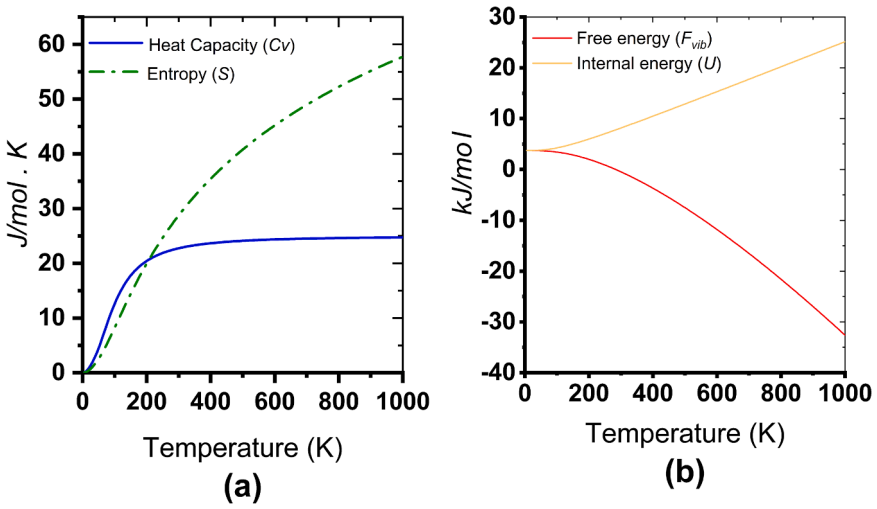

Fig. 15. The calculated temperature dependence of the (a) constant-volume heat capacity, Cv, and entropy, S, and of the (b) internal energy, U, and Helmholtz free energy, F, for Fe_2MnIn.

distortion at 0 K [88–92]. Looking at the frequencies, the maximum vibration tops out around 230 cm^{-1}. Three distinct acoustic branches emerge at the Gamma point, marking the paths of collective sound wave propagations. The optical branches, in the meantime, lie in the range of 120 cm^{-1} to 230 cm^{-1}. It is interesting to note that the absence of a sharp phonon bandgap indicates a large level of "talk" or interaction between the optical and acoustic vibrations. By checking the atom-resolved density of states (DOS), we see a clear picture of how atomic mass shapes this vibrational landscape. Heavier In atoms mostly dictate the lower-frequency acoustic regime, yet it is the lighter Fe and Mn atoms that drive the higher-frequency optical modes. The fact that the Fe and Mn states overlap so significantly suggests the crystal structure is held together by quite robust metallic bonding.

4. Conclusion

To summarize, a systematic characterization of the physical properties belonging to the Fe_2MnIn full-Heusler alloy was performed through first-principles calculations. The results show the inverse (X_a) structure to be the preferred arrangement, including energetic, thermodynamic, and mechanical stability. The compound's half-metallic ferromagnetism is established by electronic analysis, where the mBJ potential is found to provide a more accurate and wider minority-spin gap. The resultant electronic architecture makes 100% spin polarization possible, thus creating an obvious pathway to maximizing the performance efficiency of spintronic devices. Furthermore, results from elasticity calculations indicate the compound is mechanically stable and possesses ductile attributes. The structural durability required for thin-film applications is guaranteed by the high Young's modulus and anisotropy observed. The Fe_2MnIn optical properties are investigated to have spin-polarized anisotropy with a 38% rise in the refractive index in the form of the static index observed in optical modeling with mBJ. Finally, the thermodynamic characteristic of the material suggests great robust lattice stability. This is evidenced by the specific heat capacity hitting the classical 3R limit and a high Debye temperature. Overall, the combination of a half-metallic ground state, a stable ferromagnetic phase, and convenient mechanical ductility of Fe_2MnIn makes it an extremely useful material system in the development of next-wave spin-based electronics. The underlying principles of these findings must be subjected to direct experimentation for final proof.

CRediT authorship contribution statement

Salma Braik: Writing – original draft, Software, Methodology, Investigation, Formal analysis, Data curation. **Hasan A. Masri:** Writing – review & editing, Visualization, Validation, Supervision, Software, Resources, Methodology, Investigation, Formal analysis, Data curation. **Nazia Iram:** Writing – original draft, Validation, Supervision, Software, Resources, Methodology, Investigation, Formal analysis, Data curation. **Mohammed S. Abu-Jafar:** Writing – review & editing, Visualization, Validation, Supervision, Software, Project administration, Methodology, Conceptualization. **Noorhan F. AlShaikh Mohammad:** Writing –

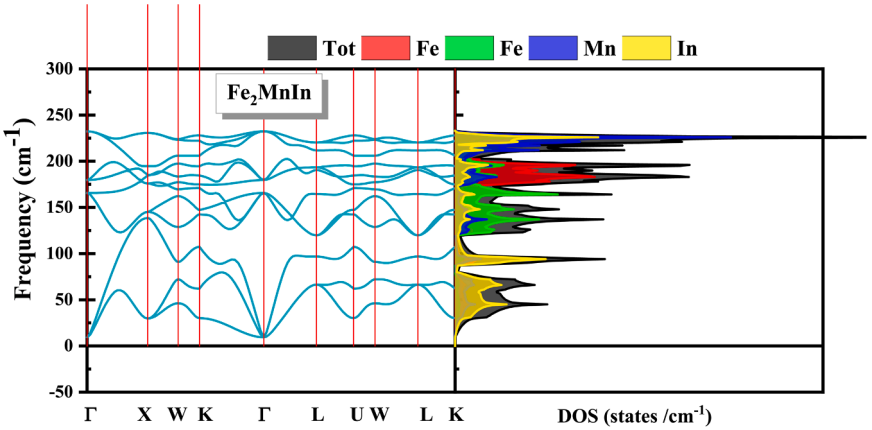

Fig. 16. Phonon dispersion curves and atom-resolved phonon density of states (PhDOS) for the $L2_1$ cubic Fe_2MnIn Heusler alloy.

original draft, Software, Methodology, Investigation, Formal analysis, Data curation. **Jihad Asad:** Writing – original draft, Software, Methodology, Investigation, Formal analysis, Data curation. **Mahmoud Farout:** Writing – original draft, Software, Methodology, Investigation, Formal analysis, Data curation. **Mohammed Yasin:** Writing – original draft, Software, Methodology, Investigation, Formal analysis, Data curation. **Aman Kumar:** Writing – original draft, Software, Methodology, Investigation, Formal analysis, Data curation. **Ahmad A. Mousa:** Writing – original draft, Software, Methodology, Investigation, Formal analysis, Data curation. **Saber Saad Essaoud:** Writing – original draft, Software, Methodology, Investigation, Formal analysis, Data curation.

Declaration of competing interest

No conflict of interest exists in the submission of the article.

Data availability

Data will be made available on request.

References

[1] S. Twaha, J. Zhu, Y. Yan, B. Li, A comprehensive review of thermoelectric technology: materials, applications, modelling and performance improvement, Renew. Sustain. Energy Rev. 65 (2016) 698–726, https://doi.org/10.1016/j.rser.2016.07.034.

[2] A.A. Kadhim, J.M. Khalaf Al-zyadi, M.A. Nattiq, First-principles calculations to investigate structural, electrical, and optical properties of half Heusler alloy LiCrN, Phys. Lett. A 442 (2022) 128178, https://doi.org/10.1016/j.physleta.2022.128178.

[3] J.M. Khalaf Al-zyadi, W.A. Abed, A.H. Ati, Electronic and magnetic properties of bulk and surfaces half-Heusler alloy KCaB and its bulk thermoelectric properties, Int. J. Mod. Phys. B 35 (2021) 35, https://doi.org/10.1142/S0217979221502581.

[4] J.M. Khalaf Al-zyadi, H.I. Asker, Preserving the half-metallicity at the full Heusler alloy Sc2CrSi surfaces as well as Sc2CrSi/HgTe (1 1 1) interface, J. Magn. Magn. Mater. 539 (2021) 168371, https://doi.org/10.1016/j.jmmm.2021.168371.

[5] M.N. Baibich, J.M. Broto, A. Fert, F.N. Van Dau, F. Petroff, P. Etienne, G. Creuzet, A. Friederich, J. Chazelas, Giant magnetoresistance of (001)Fe/(001)Cr magnetic superlattices, Phys. Rev. Lett. 61 (1988) 2472–2475, https://doi.org/10.1103/PhysRevLett.61.2472.

[6] A.A. Kadhim, H. Sedghi, J.M.K. Al-zyadi, Investigation of structural, electronic, and optical properties of bulk and monolayer for new material CrS under electric field effect, J. Magn. Magn. Mater. 603 (2024) 172276, https://doi.org/10.1016/j.jmmm.2024.172276.

[7] A. Telegin, Y. Sukhorukov, Magnetic semiconductors as materials for spintronics, Magnetochemistry 8 (2022) 173, https://doi.org/10.3390/magnetochemistry8120173.

[8] G. Schmidt, Concepts for spin injection into semiconductors—a review, J. Phys. D 38 (2005) R107–R122, https://doi.org/10.1088/0022-3727/38/7/R01.

[9] O. Örnek, A. İyigör, A.S. Meriç, M. Çanlı, M. Özduran, N. Arıkan, First-principle investigations of (Ti1 – xVx)2FeGa alloys. A study on structural, Magnetic, electronic, and elastic properties, Russ. J. Phys. Chem. A 95 (2021) 2592–2599, https://doi.org/10.1134/S003602442113015X.

[10] N. Arıkan, A. İyigör, A. Candan, Ş. Uğur, Z. Charifi, H. Baaziz, G. Uğur, Electronic and phonon properties of the full-Heusler alloys X2YAl (X = Co, Fe and Y = Cr, Sc): a density functional theory study, J. Mater. Sci. 49 (2014) 4180–4190, https://doi.org/10.1007/s10853-014-8113-7.

[11] F. Heusler, F. Richarz, Studien über magnetisierbare manganlegierungen, Z. Anorgan. Chem. 61 (1909) 265–279, https://doi.org/10.1002/zaac.19090610121.

[12] R.J. Quinn, J.-W.G. Bos, Advances in half-Heusler alloys for thermoelectric power generation, Mater. Adv. 2 (2021) 6246–6266, https://doi.org/10.1039/D1MA00707F.

[13] S. Kumar, Diwaker, S.L. Gupta, K.S. Vinayak, Ab initio study of the newly proposed full Heusler alloy Co2CuAl : insights from DFT, Mater. Today Proc. (2023), https://doi.org/10.1016/j.matpr.2023.03.105.

[14] A. Jabar, S. Idrissi, L. Bahmad, Study of the physical properties of the full Heusler Nb2RuSi alloy using first-principles calculations, Solid. State Commun. 381 (2024) 115446, https://doi.org/10.1016/j.ssc.2024.115446.

[15] R.S. Sunmonu, J.O. Akinlami, E.O. Dare, G.A. Adebayo, Effects of Y atom substitution on the structural, magnetic, electronic, elastic, mechanical, thermodynamic and thermoelectric properties of Co2YAl (Y = Cr, Mn) Full Heusler alloys from first principles investigations, Comput. Cond. Matter 21 (2019) e00412, https://doi.org/10.1016/j.cocom.2019.e00412.

[16] M. Shakil, S. Mushtaq, I. Zeba, S.S.A. Gillani, M.I. Khan, H. Arshad, M. Rafique, Structural, electronic, magnetic and thermoelectric properties of full heusler alloys Co2YZ (Z = S, Ge, Se): a first principles calculation, Physica B 602 (2021) 412558, https://doi.org/10.1016/j.physb.2020.412558.

[17] X.-P. Wei, Y.-H. Zhou, First-principles and Monte Carlo studies of the Fe2NiZ compounds on exchange interactions and Curie temperatures, Intermetallics 93 (2018) 283–289, https://doi.org/10.1016/j.intermet.2017.10.006.

[18] S. Berri, Thermoelectric properties of A2BCl6: a first principles study, J. Phys. Chem. Solids 170 (2022) 110940, https://doi.org/10.1016/j.jpcs.2022.110940.

[19] M. Markov, X. Hu, H.-C. Liu, N. Liu, S.J. Poon, K. Esfarjani, M. Zebarjadi, Semi-metals as potential thermoelectric materials, Sci. Rep. 8 (2018) 9876, https://doi.org/10.1038/s41598-018-28043-3.

[20] K. Zhang, Y. Feng, Y. Chen, J. Gong, L. Xu, Z. Wu, C. Liu, C. Chen, K. Shimada, L. Qiao, Spin-momentum locking in locally noncentrosymmetric quantum materials, Rep. Prog. Phys. 88 (2025) 106503, https://doi.org/10.1088/1361-6633/ae1379.

[21] T. Roy, D. Pandey, A. Chakrabarti, Probing the possibility of coexistence of martensite transition and half-metallicity in Ni and Co-based full-Heusler alloys: an *ab initio* calculation, Phys. Rev. B 93 (2016) 184102, https://doi.org/10.1103/PhysRevB.93.184102.

[22] V. Sokolovskiy, O.N. Miroshkina, A. Sanosyan, D. Baigutlin, V. Buchelnikov, M. E. Gruner, Magnetic and structural properties of Co-Ni-Z=(Z Al, Ga, In, Sn) Heusler alloys: effect of structural motives and chemical disorder, J. Magn. Magn. Mater. 546 (2022) 168728, https://doi.org/10.1016/j.jmmm.2021.168728.

[23] D. Mahata, A. Srinivasan, Stabilization of various structural phases and magnetic properties of chemically synthesized Co-Ni-Ga nanoparticles, Materialia 35 (2024) 102116, https://doi.org/10.1016/j.mtla.2024.102116.

[24] H.A. Masri, M.S. Abu-Jafar, A. Bouhemadou, N. Baadji, Multifunctional properties of FeMnScAl quaternary Heusler alloy: insights into spintronics, photovoltaics, and thermoelectric applications, J. Phys. Chem. C 129 (2025) 2672–2690, https://doi.org/10.1021/acs.jpcc.4c06553.

[25] H.A. Masri, M.S. Abu-Jafar, N.F.A. Mohammad, S.S. Essaoud, Extensive DFT study of FeMnCrGe quaternary Heusler alloy: structural, elastic, magnetic, optical and thermoelectric properties, Opt. Quantum. Electron. 57 (2025) 139, https://doi.org/10.1007/s11082-024-08029-4.

[26] S. Noui, Z. Charifi, H. Baaziz, G. Uğur, Ş. Uğur, Effect of structure on the electronic, magnetic and thermal properties of cubic Fe2MnxNi1−xSi Heusler alloys, J. Electron. Mater. 48 (2019) 337–351, https://doi.org/10.1007/s11664-018-6704-9.

[27] R. Golesorkhtabar, P. Pavone, J. Spitaler, P. Puschnig, C. Draxl, ElaStic: a tool for calculating second-order elastic constants from first principles, Comput. Phys. Commun. 184 (2013) 1861–1873, https://doi.org/10.1016/j.cpc.2013.03.010.

[28] I.N. Frantsevich, F.F. Voronov, S.A. Bokuta, Elastic Constants and Elastic Moduli of Metals and Insulators Handbook, 1983.

[29] C.M. Zener, S. Siegel, Elasticity and anelasticity of metals, J. Phys. Colloid. Chem. 53 (1949) 1468, https://doi.org/10.1021/j150474a017.

[30] F. Birch, Finite elastic strain of cubic crystals, Phys. Rev. 71 (1947) 809–824, https://doi.org/10.1103/PhysRev.71.809.

[31] B. Dahal, A. Al Maruf, S. Prophet, Y. Huh, P.V. Lukashev, P. Kharel, Electronic, magnetic, and structural properties of Fe2MnSn Heusler alloy, AIP. Adv. 10 (2020), https://doi.org/10.1063/1.5127671.

[32] Y. Jirásková, J. Buršík, D. Janičkovič, O. Životský, Influence of preparation technology on microstructural and magnetic properties of Fe2MnSi and Fe2MnAl Heusler alloys, Materials 12 (2019) 710, https://doi.org/10.3390/ma12050710.

[33] S. Yoshimura, H. Kobayashi, G. Egawa, H. Saito, S. Ishida, Acceleration of ordering transformation of a new Fe2(Mn,Cr)Si Heusler-alloy film by very high frequency plasma irradiation process during radio frequency sputter deposition, J. Appl. Phys. 109 (2011), https://doi.org/10.1063/1.3562198.

[34] W. Cheng, J. Dong, L. Wei, G. Shen, Q. Wang, R. Sun, Magnetically responsive intelligent fibers: nano-engineered materials and multifunctional integration for advanced applications, Mater. Horiz. 12 (2025) 9870–9892, https://doi.org/10.1039/D5MH01383F.

[35] W. Kohn, L.J. Sham, Self-consistent equations including exchange and correlation effects, Phys. Rev. 140 (1965) A1133–A1138, https://doi.org/10.1103/PhysRev.140.A1133.

[36] S. Blügel, G. Bihlmayer, Full-potential linearized augmented planewave method, Comput. Nanosci. 31 (2006) 85–129. https://juser.fz-juelich.de/record/50026/files/FZJ-2014-02213.pdf (Accessed 15 August 2024).

[37] P. Blaha, K. Schwarz, P. Sorantin, S.B. Trickey, Full-potential, linearized augmented plane wave programs for crystalline systems, Comput. Phys. Commun. 59 (1990) 399–415, https://doi.org/10.1016/0010-4655(90)90187-6.

[38] P. Blaha, K. Schwarz, F. Tran, R. Laskowski, G.K.H. Madsen, L.D. Marks, WIEN2k: an APW+lo program for calculating the properties of solids, J. Chem. Phys. 152 (2020), https://doi.org/10.1063/1.5143061/16727314/074101_1_ACCEPTED_MANUSCRIPT.PDF.

[39] J.A. Camargo-Martínez, R. Baquero, Performance of the modified Becke-Johnson potential for semiconductors, Phys. Rev. B 86 (2012) 195106, https://doi.org/10.1103/PHYSREVB.86.195106/FIGURES/2/MEDIUM.

[40] T.M. Bhat, S. Singh, D.C. Gupta, Electronic and transport properties of LaNi4Sb12 skutterudite: modified Becke–Johnson approach, J. Electron. Mater. 47 (2018) 4544–4549, https://doi.org/10.1007/s11664-018-6323-5.

[41] F. Tran, P. Blaha, Accurate band gaps of semiconductors and insulators with a semilocal exchange-correlation potential, Phys. Rev. Lett. 102 (2009) 226401, https://doi.org/10.1103/PhysRevLett.102.226401.

[42] F.D. Murnaghan, The compressibility of media under extreme pressures, Proc. Natl. Acad. Sci. USA 30 (1944) 244–247, https://doi.org/10.1073/pnas.30.9.244.

[43] T. Charpin, A Package for Calculating Elastic Tensors of Cubic Phase Using WIEN, Laboratory of Geometrix, Paris, 2001, pp. 1–21.

[44] C. Ambrosch-Draxl, J.A. Majewski, P. Vogl, G. Leising, First-principles studies of the structural and optical properties of crystalline poly(*para* -phenylene), Phys. Rev. B 51 (1995) 9668–9676, https://doi.org/10.1103/PhysRevB.51.9668.
[45] C. Ambrosch-Draxl, J.O. Sofo, Linear optical properties of solids within the full-potential linearized augmented planewave method, Comput. Phys. Commun. 175 (2006) 1–14, https://doi.org/10.1016/j.cpc.2006.03.005.
[46] P. Giannozzi, S. Baroni, N. Bonini, M. Calandra, R. Car, C. Cavazzoni, D. Ceresoli, G.L. Chiarotti, M. Cococcioni, I. Dabo, A. Dal Corso, S. de Gironcoli, S. Fabris, G. Fratesi, R. Gebauer, U. Gerstmann, C. Gougoussis, A. Kokalj, M. Lazzeri, L. Martin-Samos, N. Marzari, F. Mauri, R. Mazzarello, S. Paolini, A. Pasquarello, L. Paulatto, C. Sbraccia, S. Scandolo, G. Sclauzero, A.P. Seitsonen, A. Smogunov, P. Umari, R.M. Wentzcovitch, QUANTUM ESPRESSO: a modular and open-source software project for quantum simulations of materials, J. Phys. 21 (2009) 395502, https://doi.org/10.1088/0953-8984/21/39/395502.
[47] S.M. Azar, A.A. Mousa, J.M. Khalifeh, Structural, electronic and magnetic properties of Ti1+xFeSb Heusler alloys, Intermetallics 85 (2017) 197–205, https://doi.org/10.1016/J.INTERMET.2017.02.018.
[48] A. Reuss, Berechnung der Fließgrenze Von Mischkristallen auf grund der plastizitätsbedingung für einkristalle, ZAMM 9 (1929) 49–58, https://doi.org/10.1002/ZAMM.19290090104.
[49] M. Born, K. Huang, Dynamical Theory of Crystal Lattices, Oxford University Press, New York, NY, 1996, https://doi.org/10.1093/oso/9780192670083.001.0001.
[50] S.F. Pugh, XCII. Relations between the elastic moduli and the plastic properties of polycrystalline pure metals, Lond. Edinb. Dubl. Philos. Mag. J. Sci. 45 (1954) 823–843, https://doi.org/10.1080/14786440808520496.
[51] J.W. Soh, H.M. Lee, H.S. Kwon, Relation between Poisson's ratio and ionicity in simple binary cubic compounds, J. Alloys Compd. 194 (1993) 119–125, https://doi.org/10.1016/0925-8388(93)90656-8.
[52] P. Ravindran, L. Fast, P.A. Korzhavyi, B. Johansson, J. Wills, O. Eriksson, Density functional theory for calculation of elastic properties of orthorhombic crystals: application to TiSi2, J. Appl. Phys. 84 (1998) 4891–4904, https://doi.org/10.1063/1.368733.
[53] D. Jiang, M. Wu, D. Liu, F. Li, M. Chai, S. Liu, Structural stability, electronic structures, mechanical properties and debye temperature of transition metal impurities in tungsten: a first-principles study, Metals 9 (2019) 967, https://doi.org/10.3390/met9090967.
[54] S. Skaftouros, K. Özdoğan, E. Şaşioğlu, I. Galanakis, Generalized Slater-Pauling rule for the inverse Heusler compounds, Phys. Rev. B 87 (2013) 024420, https://doi.org/10.1103/PHYSREVB.87.024420/FIGURES/3/MEDIUM.
[55] I. Galanakis, P.H. Dederichs, N. Papanikolaou, Slater-Pauling behavior and origin of the half-metallicity of the full-Heusler alloys, Phys. Rev. B 66 (2002) 174429, https://doi.org/10.1103/PhysRevB.66.174429.
[56] J.P. Perdew, K. Burke, M. Ernzerhof, Generalized gradient approximation made simple, Phys. Rev. Lett. 77 (1996) 3865–3868, https://doi.org/10.1103/PhysRevLett.77.3865.
[57] C. Felser, G.H. Fecher, B. Balke, Spintronics: a challenge for materials science and solid-state chemistry, Angew. Chem. Int. Ed. 46 (2007) 668–699, https://doi.org/10.1002/ANIE.200601815.
[58] R.G. Pearson, Electronegativity scales, Acc. Chem. Res. 23 (1990) 1–2, https://doi.org/10.1021/ar00169a001.
[59] T. Graf, C. Felser, S.S.P. Parkin, Simple rules for the understanding of Heusler compounds, Prog. Solid State Chem. 39 (2011) 1–50, https://doi.org/10.1016/J.PROGSOLIDSTCHEM.2011.02.001.
[60] K. Özdoğan, E. Şaşioğlu, I. Galanakis, Slater-Pauling behavior in LiMgPdSn-type multifunctional quaternary Heusler materials: half-metallicity, spin-gapless and magnetic semiconductors, J. Appl. Phys. 113 (2013), https://doi.org/10.1063/1.4805063/370344.
[61] S. Wurmehl, G.H. Fecher, H.C. Kandpal, V. Ksenofontov, C. Felser, H.-J. Lin, J. Morais, Geometric, electronic, and magnetic structure of Co2 FeSi: Curie temperature and magnetic moment measurements and calculations, Phys. Rev. B 72 (2005) 184434, https://doi.org/10.1103/PhysRevB.72.184434.
[62] Z. Zada, A.A. Khan, A.H. Reshak, I. khan, S. Zada, M. Ismail, M. Fazal-ur-Rehman, M. Saqib, G. Murtaza, Q. Khan, M.M. Ramli, Insight into the electronic structure, magnetic, and thermoelectric properties of transition metal pnictides KCr2L2 (K= Ca, Sr; L = P, As): as substitute source for renewing energy, Physica B 649 (2023) 414470, https://doi.org/10.1016/j.physb.2022.414470.
[63] Z. Zada, R. Zada, A.A. Khan, M. Saqib, M.F.U. Rehman, M. Ismail, N. Kulhari, K. S. Sharma, M. Ismail, X. Shen, M. Faizan, Investigation of electronic structure, magnetic stability, spin coupling, and thermodynamic properties of novel antiferromagnets XMn2Y2 (X = Ca, Sr; Y = P, As), J. Mol. Struct. 1268 (2022) 133698, https://doi.org/10.1016/j.molstruc.2022.133698.
[64] R. Piercy, N.A. Hampson, The electrochemistry of indium, J. Appl. Electrochem. 5 (1975) 1–15, https://doi.org/10.1007/BF00625955.
[65] L. Bainsla, K.G. Suresh, Equiatomic quaternary Heusler alloys: a material perspective for spintronic applications, Appl. Phys. Rev. 3 (2016) 031101, https://doi.org/10.1063/1.4959093.
[66] K. Dewhurst, S. Sharma, ELK code development, (n.d.). https://www2.mpi-halle.mpg.de/theory_department/research/elk_code_development/(Accessed 4 April 2024).
[67] T. Lantri, S. Bentata, B. Bouadjemi, W. Benstaali, B. Bouhafs, A. Abbad, A. Zitouni, Effect of Coulomb interactions and Hartree-Fock exchange on structural, elastic, optoelectronic and magnetic properties of Co2MnSi Heusler: a comparative study, J. Magn. Magn. Mater. 419 (2016) 74–83, https://doi.org/10.1016/j.jmmm.2016.06.012.
[68] S. Sharma, A.S. Verma, V.K. Jindal, Ab initio studies of structural, electronic, optical, elastic and thermal properties of silver gallium dichalcogenides (AgGaX2: X = S, Se, Te), Mater. Res. Bull. 53 (2014) 218–233, https://doi.org/10.1016/J.MATERRESBULL.2014.02.021.
[69] A. Ben Mhenni, D. Van Tuan, L. Geilen, M.M. Petrić, M. Erdi, K. Watanabe, T. Taniguchi, S.A. Tongay, K. Müller, N.P. Wilson, J.J. Finley, H. Dery, M. Barbone, Breakdown of the static dielectric screening approximation of coulomb interactions in atomically thin semiconductors, ACS Nano 19 (2025) 4269–4278, https://doi.org/10.1021/acsnano.4c11563.
[70] A. Obeidat, A. Alrousan, S. Abu-Rajouh, First-principles study of structural, hydrogen storage, mechanical, electronic, and optical properties of K2NaXH6 (X = Al, As, Bi, Ga, In) double perovskite hydrides, J. Power Sources 642 (2025) 236944, https://doi.org/10.1016/j.jpowsour.2025.236944.
[71] H. Murtaza, Q. Ain, J. Munir, H. Ullah, H.M. Ghaithan, A.A. Ali Ahmed, S.M. H. Qaid, Unveiling the mechanical, structural, thermoelectric, and optoelectronic potential of K2NaGaBr6 and K2RbTlBr6 double perovskites for sustainable technologies, Sol. Energy 273 (2024) 112502, https://doi.org/10.1016/j.solener.2024.112502.
[72] M. Rashid, Study of vanadium difluoride AVF3 (A = Na, K, Rb) for optoelectronic and thermoelectric device applications via ab initio calculations, J. Supercond. Nov. Magn. 33 (2020) 1167–1175, https://doi.org/10.1007/s10948-019-05317-z.
[73] M. Fox, Optical Properties of Solids, 2nd ed., 3, Oxford University Press, Oxford, 2010, pp. 188–211.
[74] F. Wooten, Optical Properties of Solids, Elsevier, 1972, https://doi.org/10.1016/C2013-0-07656-6.
[75] M.S. Dresselhaus, Solid State Physics Optical Properties of Solids, Srisathya Sai College Digital Library, 2022, pp. 8–50.
[76] W. Cao, M. Zhang, M. Cao, A perspective of tailoring dielectric genes for 2D materials toward advanced electromagnetic functions, Adv. Funct. Mater. 34 (2024), https://doi.org/10.1002/adfm.202410928.
[77] L. Ren, X. Wen, D. Du, Y. Yan, H. Xu, T. Zeng, C. Shu, Engineering high-spin state cobalt cations in spinel ZnCo2O4 for spin channel propagation and electrocatalytic activity enhancement in Li-O2 battery, Chem. Eng. J. 462 (2023) 142288, https://doi.org/10.1016/j.cej.2023.142288.
[78] P. Nagpal, V.I. Klimov, Role of mid-gap states in charge transport and photoconductivity in semiconductor nanocrystal films, Nat. Commun. 2 (2011) 486, https://doi.org/10.1038/ncomms1492.
[79] R. Skomski, J.M.D. Coey, Magnetic anisotropy — how much is enough for a permanent magnet? Scr. Mater. 112 (2016) 3–8, https://doi.org/10.1016/j.scriptamat.2015.09.021.
[80] R.E. Hummel, Introduction. Electronic Properties of Materials, Springer New York, New York, NY, 2011, pp. 405–407, https://doi.org/10.1007/978-1-4419-8164-6_18.
[81] A. Soussi, A. Ait Hssi, M. Boujnah, L. Boulkadat, K. Abouabassi, A. Asbayou, A. Elfanaoui, R. Markazi, A. Ihlal, K. Bouabid, Electronic and optical properties of TiO2 thin films: combined experimental and theoretical study, J. Electron. Mater. 50 (2021) 4497–4510, https://doi.org/10.1007/s11664-021-08976-8.
[82] I.M. Baker, II-VI Narrow Bandgap Semiconductors: Optoelectronics, 2017, p. 1, https://doi.org/10.1007/978-3-319-48933-9_34.
[83] J.M. Martínez-Duart, R.J. Martínez-Palma, Photodetectors and solar cells based on porous silicon, Phys. Status Solidi B 232 (2002) 81–88, https://doi.org/10.1002/1521-3951(200207)232:1<81::AID-PSSB81>3.0.CO;2-E.
[84] H. Zaari, M. Boujnah, A. El Hachimi, A. Benyoussef, A. El Kenz, Optical properties of ZnTe doped with transition metals (Ti, Cr and Mn), Opt. Quant. Electron. 46 (2014) 75–86, https://doi.org/10.1007/s11082-013-9708-y.
[85] M.A. Blanco, E. Francisco, V. Luaña, GIBBS: isothermal-isobaric thermodynamics of solids from energy curves using a quasi-harmonic Debye model, Comput. Phys. Commun. 158 (2004) 57–72, https://doi.org/10.1016/j.comphy.2003.12.001.
[86] C. Kittel, P. McEuen, Introduction to Solid State Physics, John Wiley & Sons, 2018.
[87] J.P. Abriata, D.E. Laughlin, The third law of thermodynamics and low temperature phase stability, Prog. Mater. Sci. 49 (2004) 367–387, https://doi.org/10.1016/S0079-6425(03)00030-6.
[88] D.V. Suetin, I.R. Shein, Electronic structure, mechanical and dynamical stability of hexagonal subcarbides M2C (M = Tc, Ru, Rh, Pd, Re, Os, Ir, and Pt): ab initio calculations, Phys. Solid State 60 (2018) 213–224, https://doi.org/10.1134/S1063783418020282.
[89] S.A. Khandy, J.-D. Chai, Novel half-metallic L21 structured full-Heusler compound for promising spintronic applications: a DFT-based computer simulation, J. Magn. Magn. Mater. 487 (2019) 165289, https://doi.org/10.1016/j.jmmm.2019.165289.
[90] S.A. Khandy, Inspecting the electronic structure and thermoelectric power factor of novel p-type half-Heuslers, Sci. Rep. 11 (2021) 20756, https://doi.org/10.1038/s41598-021-00314-6.
[91] S.A. Khandy, J.-D. Chai, Strain engineering of electronic structure, phonon, and thermoelectric properties of p-type half-Heusler semiconductor, J. Alloys Compd. 850 (2021) 156615, https://doi.org/10.1016/j.jallcom.2020.156615.
[92] S.A. Khandy, J.-D. Chai, Origin of pseudo gap and thermoelectric signatures of semimetallic Ru2TaGa: structural stability from phonon dynamics, mechanical, and thermodynamic predictions, J. Phys. Chem. Solids 154 (2021) 110098, https://doi.org/10.1016/j.jpcs.2021.110098.